



HAL
open science

Beyond confinement effects in Fischer-Tropsch Co/CNT catalysts

Amel Cydric Ghogia, Bruno F Machado, Simon Cayez, Ange Nzihou, Philippe Serp, Katerina Soulantica, Doan Pham Minh

► **To cite this version:**

Amel Cydric Ghogia, Bruno F Machado, Simon Cayez, Ange Nzihou, Philippe Serp, et al.. Beyond confinement effects in Fischer-Tropsch Co/CNT catalysts. *Journal of Catalysis*, 2021, 397, pp.156-171. 10.1016/j.jcat.2021.03.027 . hal-03201678

HAL Id: hal-03201678

<https://imt-mines-albi.hal.science/hal-03201678v1>

Submitted on 19 Apr 2021

HAL is a multi-disciplinary open access archive for the deposit and dissemination of scientific research documents, whether they are published or not. The documents may come from teaching and research institutions in France or abroad, or from public or private research centers.

L'archive ouverte pluridisciplinaire **HAL**, est destinée au dépôt et à la diffusion de documents scientifiques de niveau recherche, publiés ou non, émanant des établissements d'enseignement et de recherche français ou étrangers, des laboratoires publics ou privés.

Beyond confinement effects in Fischer-Tropsch Co/CNT catalysts

Amel Cydric Ghogia^{a,b,c}, Bruno F. Machado,^d Simon Cayez,^c Ange Nzihou^a, Philippe Serp^{b},
Katerina Soulantica^{c*}, Doan Pham Minh^{a*}*

^a Université de Toulouse, IMT Mines Albi, UMR CNRS 5302, Centre RAPSODEE, Campus
Jarlard, F-81013 Albi, cedex 09, France.

^b LCC, CNRS-UPR 8241, ENSIACET, Université de Toulouse, France.

^c LPCNO, Université de Toulouse, CNRS, INSA, UPS, Toulouse.

^d Laboratory of Separation and Reaction Engineering - Laboratory of Catalysis and Materials
(LSRE-LCM), Chemical Engineering Department, Faculty of Engineering, University of
Porto, Rua Dr. Roberto Frias s/n, 4200-465 Porto, Portugal

Corresponding author: philippe.serp@ensiacet.fr; ksoulant@insa-toulouse.fr;

doan.phamminh@mines-albi.fr

Keywords: Cobalt catalysts; Carbon nanotubes; Fischer-Tropsch synthesis; Confinement;
Spillover

Abstract: Fischer-Tropsch catalyst preparation parameters, such as cobalt precursor and impregnation solvent, determine structure and *in fine* catalytic performances of Co-based catalysts. Co particles of 3-7 nm mean size were prepared by incipient wetness impregnation on surface-oxidized CNT. In this work the crucial impact of the chemistry operating between the Co precursor and the support during catalyst preparation on the catalyst properties is demonstrated and the influence of CNT surface chemistry on catalyst characteristics has been assessed. Very good correlations were found between: i) the reduction degree of the catalysts and the concentration of the Co(OOC-) surface species; ii) the Co_{hcp}/Co_{fcc} ratio and the amount of CO-releasing groups on the support surface; iii) the extent of hydrogen spillover and the concentration of quinone surface groups. The initial catalytic activity could only be correlated to a combination of catalyst features: percentage of Co_{hcp} , Co confinement, hydrogen spillover, and surprisingly the inverse of the Co initial particle size. No significant differences in S_{C5+} selectivity were observed, in accordance with comparable final Co particle size. Finally, the stability of the catalyst can be correlated with the initial Co particle size and the percentage of Co_{hcp} in the catalyst. These results confirm the significant impact of the precursor/support couple on the structure and performance of Co/CNT catalysts, and reveal for the first time an inverse correlation between Co particle size and activity, which is attributed to the confined Co_{hcp} phase.

1 **1. Introduction**

2 The Fischer-Tropsch synthesis (FTS) is a catalytic process enabling the conversion of syngas
3 (CO/H₂) into higher hydrocarbons, which can be upgraded into liquid fuels. Today, this process
4 becomes particularly attractive due to the stringency of environmental regulations, the decrease
5 of fossil fuel reserves, the development of biomass derived syngas technologies as well as the
6 ever increasing awareness of citizens on the utilization and benefits of sustainable fuels [1]. To
7 conduct FTS at low temperatures (*LTFT*, 220-260°C) [2], cobalt-based catalysts are particularly
8 interesting since they are more active and stable than the iron-based ones, and much cheaper
9 than the ruthenium ones [3–5]. Oxide supports such as SiO₂, Al₂O₃ or TiO₂ are generally
10 employed to stabilize cobalt particles, but they present the drawback of undesirable strong
11 cobalt-support interactions that lead to the formation of non-reducible and inactive mixed metal
12 oxides [4]. Such detrimental interactions can be circumvented by using carbon materials as
13 support modifier [6,7] or directly as support [8], since their interaction with cobalt is weaker,
14 which facilitates metal reduction. Additionally, the good thermal conductivity of some *sp*²
15 carbon materials, such as carbon nanotubes (CNT) enables to limit methane formation and
16 catalyst deactivation, by avoiding the formation of hot spots resulting from the high
17 exothermicity of the FT reaction.

18 The principal identified Co/C catalyst features influencing the catalyst performances are: i) the
19 Co particle size; ii) the Co reducibility; iii) the cobalt phase (*fcc* or *hcp*); and iv) the confinement
20 of cobalt particles (particularly in CNT) [8]. Recently, we also reported that hydrogen spillover
21 from the cobalt particles to the carbon support can also contribute to the enhancement of Co/C
22 catalytic activity [9]. All these features, which are fixed either during catalyst preparation or
23 during catalysis, can in turn be dictated by specific properties of the carbon support, such as the
24 strength of the metal-support interaction (MSI), the support textural properties, its surface
25 chemistry, its thermal stability and its conductivity [10]. Among the different methods for Co/C

1 catalyst preparation, the incipient wetness impregnation (IWI) is by far the most popular since:
2 i) it is relatively fast and inexpensive, and ii) small particle size and narrow particle distribution
3 are usually obtained. Among the different carbon supports investigated for FTS, oxidized CNT
4 have been particularly studied since they offer the additional possibility of confinement of the
5 active phase [8,10]. Furthermore, it was demonstrated that oxidized CNT show catalytic activity
6 towards CO hydro-deoxygenation reaction to yield long chain hydrocarbons similar to FTS
7 [11].

8 Another important parameter to consider during catalyst preparation is the choice of the cobalt
9 precursor and of the impregnating solvent. The decomposition of the cobalt precursor is a
10 crucial step in Co-based catalyst preparation, and a slow decomposition rate favors small Co
11 particle size [8]. Cobalt acetate and cobalt nitrate precursors are the most commonly used.
12 However, the data available in the literature are insufficient to explain the effect of cobalt
13 precursors in the case of Co/C catalysts. Xiong *et al.* [12] prepared Co_N/CNT and Co_A/CNT (15
14 wt.%) catalysts using cobalt nitrate (Co_N) and cobalt acetate (Co_A) precursors by the IWI
15 method. The Co_N/CNT catalyst ($d_{Co} = 3.9$ nm) was slightly more active than the Co_A/CNT
16 catalyst ($d_{Co} = 4.4$ nm) in FTS. However, in another study [13], Co catalysts prepared on
17 activated carbon or oxidized diamonds as supports from cobalt acetate, were more active than
18 those prepared from cobalt nitrate. These contradictory results could be related to the nature of
19 the supports. Additionally, the solvent used during the catalyst preparation allows not only
20 dissolving the precursor and promoting its contact with the support, but also controlling the
21 final catalyst structure. The interaction between the cobalt precursor and the support depends
22 on the solvent surface tension, which controls support wettability [8]. De Jong and coworkers
23 compared water and ethanol as solvents for the impregnation of CNT with cobalt nitrate [14].
24 The catalytic results showed that the catalysts prepared in ethanol (Co_{N-E}/CNT) presented a
25 superior cobalt-weight based activity over those prepared from an aqueous solution (Co_N.

1 w/CNT), because the cobalt particles had grown less during reduction and FTS, leading to
2 higher specific metal surface areas. However, in most of these studies, not all the features
3 influencing the catalyst performances have been considered for the rationalization of the
4 catalyst activity.

5 In the present study, the influence of cobalt precursor (nitrate or acetate) and the impregnation
6 solvent (water or ethanol) on the structure of Co/CNT catalysts prepared by IWI is studied. We
7 intend for the first time at drawing structure/performances correlations considering all the
8 features known to influence the catalyst performances, that is: Co particle confinement, Co
9 particle size, Co reducibility, Co crystallographic phase, and hydrogen spillover.

10 **2. Experimental section**

11 **2.1 Catalyst preparation**

12 The CNT were synthesized at 650 °C by catalytic chemical vapor deposition in a fluidized bed
13 reactor using ethylene (C_2H_4) as a carbon source and an AlFeCoO_4 catalyst [15]. The CNT were
14 purified using an aqueous solution (50 vol% H_2SO_4) under reflux at 140 °C for 3 h. The purified
15 CNT were further oxidized with HNO_3 under reflux at 140 °C for 3 h. The oxidized CNT
16 contain 1.3 % w/w of catalyst residue (TGA analysis, Figure S1) consisting in FeCo
17 nanoparticles, which are encapsulated in carbon, thus, not catalyzing the FTS (EDX analysis,
18 Figure S1).

19 The cobalt catalysts were prepared by incipient wetness impregnation (IWI) with a solution of
20 either cobalt acetate ($\text{Co}(\text{CH}_3\text{COO})_2 \cdot 4\text{H}_2\text{O}$ 97%) or cobalt nitrate ($\text{Co}(\text{NO}_3)_2 \cdot 6\text{H}_2\text{O}$ 99%). A
21 cobalt loading of 15% on the carbon support was targeted. First, 2 g of oxidized CNT were
22 dried at 120 °C for 1 h under dynamic vacuum. Then, the solution containing cobalt acetate
23 (1.54 g $\text{Co}(\text{CH}_3\text{COO})_2 \cdot 4\text{H}_2\text{O}$, in 10 mL of water or ethanol-water mixture) or cobalt nitrate

1 (1.76 g Co(NO₃)₂·6H₂O 99%, in 10 mL of water or ethanol) were introduced and sonicated for
2 20 min. Then, four cycles of 10 min sonication (one every hour) were performed under static
3 vacuum in order to complete the impregnation. Finally, the solid was dried at 120 °C overnight
4 and calcined under argon flow at 350 °C for 3 h with a heating rate of 2 °C.min⁻¹. The resulting
5 catalysts were denoted Co_{N-W}/CNT (*N* = nitrate; *W* = water), Co_{N-E}/CNT (*N* = nitrate; *E* =
6 ethanol), Co_{A-W}/CNT (*A* = acetate; *W* = water), and Co_{A-EW}/CNT (*A* = acetate; *EW* = ethanol-
7 water mixture).

8 **2.2 Material characterization**

9 Dynamic Vapor Sorption (DVS) was used to measure the sorption of water and ethanol on the
10 CNT at 25 °C, using a device from Surface Measurement Systems. The temperature of the
11 chamber and the nitrogen gas flow were set at 25 °C and 500 mL.min⁻¹, respectively. 0.1 g of
12 sample was used for the measurements. The isothermal stages were: i) drying level, circulation
13 of dry nitrogen gas for 60 min; ii) 10% RH (relative humidity) from 0% to 90% RH; and iii)
14 95% RH. The water or ethanol content at equilibrium was determined according to the relative
15 humidity as follows (Eq. 1):

$$16 \quad g_{ads} g_{CNT}^{-1} = \left(\frac{m_s}{m_p} \right) \quad \text{(Eq. 1)}$$

17 Where m_s is the mass of the solvent adsorbed on the CNT, and m_p is the mass of dry CNT.

18 A JEOL JEM-1011 microscope equipped with a tungsten thermionic electron source and with
19 an acceleration voltage of 100 kV was used for routine TEM observations. A JEOL JEM 2100F-
20 EDS microscope with an acceleration voltage of 200 kV was used for high-resolution
21 transmission electron microscopy (HRTEM) observations. The particle size distribution of
22 fresh and spent catalysts was determined by TEM. At least 300 Co particles were measured for
23 each sample. For TEM analyses, catalyst samples were prepared by ultrasound-assisted

1 dispersion in pure ethanol, and the suspensions were dropped onto a collodion carbon covered
2 copper film. The filling yield was calculated by counting the particles deposited inside and on
3 the outer surface of 40 different CNT (about 300 Co particles). The yield (Eq. 2) was calculated
4 as follows [16]:

$$5 \quad \text{Yield} = 2 \left(\frac{\text{number of particles inside}}{\text{Total number of particles}} \times 100 \right) - 100 \quad (\text{Eq. 2})$$

6 The specific surface area, and pore size distribution were determined from N₂
7 adsorption/desorption isotherms at - 196 °C by using a Micromeritics instrument. Prior to
8 analysis, all samples were degassed under vacuum at 120 °C for 6 h.

9 The crystalline structure and the crystallite size of the fresh catalysts were determined by X-ray
10 diffraction (XRD). Before analysis, the catalysts were reduced under 40%H₂/Ar flow for 2 h at
11 350 °C with a heating rate of 5 °C.min⁻¹. The standard XRD measurements were performed on
12 a Bragg-Brentano configuration (θ-θ) EMPYREAN diffractometer equipped with a cobalt
13 anode fed at 35 kV and 45 mA. The radiation generated by the anode has an average wavelength
14 (K_α) λ = 1.79 Å. The analysis was carried with an angular domain 2θ between 10 and 120°, a
15 step of 0.07 °/s and an acquisition time of 200 s. For the *in-situ* XRD, the heating oven was
16 mounted on the diffractometer, followed by the introduction of the sample into the heating
17 chamber. Using a gas composition of 5%H₂ in N₂, the furnace chamber was purged at 1 bar for
18 four vacuum-5%H₂/N₂ cycles. The catalyst was progressively reduced (from Co₃O₄ to Co⁰) in
19 the furnace under a 5%H₂/N₂ flow from 30 °C to 800 °C with a heating rate of 5 °C. min⁻¹ and
20 diffractograms were recorded at various temperatures. The Co crystallite size of the fresh
21 catalysts was determined using the Scherrer equation [17] and the HighScore software, while
22 the crystalline structure of the spent catalysts was determined by MAUD software. Rietveld
23 refinement was also applied to quantify the different crystalline phases.

1 The thermogravimetric analysis was performed with a TGA/DSC Shimadzu apparatus. The
2 measurements were carried out from 25 to 350 °C under nitrogen flow of 20 mL.min⁻¹ with a
3 heating rate of 2 °C.min⁻¹, with a plateau time of 3 h at 350°C.

4 The X-ray photoelectron spectroscopy (XPS) was performed using a monochromatized Al K_α
5 (hν = 1486.6 eV) source on a ThermoScientific K_α system. The X-ray spot size was about 400
6 μm. The pass energy was fixed at 30 eV with a step of 0.1 eV for core levels and 160 eV for
7 surveys (step 1eV). The spectrometer energy calibration was done using the Au 4f_{7/2} (83.9 ± 0.1
8 eV) and Cu 2p_{3/2} (932.8 ± 0.1 eV) photoelectron lines. XPS spectra were recorded in direct
9 mode N(Ec) and the background signal was removed using the Shirley method [18].

10 Magnetic measurements were performed using a Quantum Design Vibrating Sample
11 Magnetometer (VSM) at 300 K and 5 K and field up to 5 T [19]. This technique makes it
12 possible to determine the saturation magnetization (M_s, Eq. 3) of a sample of catalyst under the
13 effect of a magnetic field and to deduce its reducibility knowing the saturation magnetization
14 of the bulk cobalt (M_s bulk, equal to 163 emu g_{Co}⁻¹).

$$15 \quad M_s \text{ sample (emu g}_{Co}^{-1}) = \frac{M_s(VSM)}{m_{cat} \times \%Co} \quad (Eq. 3)$$

16 With M_s (VSM) the magnetization obtained by the equipment, m_{cat} the mass of the catalyst and
17 %_{Co} the cobalt content obtained by ICP. This allows the determination of the reduction degree
18 of cobalt (Eq. 4).

$$19 \quad \text{Reduction degree (\%)} = \frac{M_s \text{ sample}}{M_s \text{ bulk}} \times 100 \quad (Eq. 4)$$

20 The measurements were performed on reduced catalysts. Before analysis, the catalysts were
21 reduced in 40%H₂/Ar flow for 8 h at 350 °C with a heating rate of 5 °C.min⁻¹. Standard VSM

1 (Vibrating Sample Magnetometry) capsules were filled with an exactly weighted amount (a few
2 mg) of sample and sealed. To avoid any accidental oxidation, the samples were prepared in a
3 glovebox, and transferred to the cryostat in a Schlenk vessel. The VSM capsule containing the
4 sample is rapidly introduced into the VSM in order to avoid air exposure. For each catalyst, two
5 measurements were performed. A first hysteresis cycle was performed at 300 K (27 °C) and the
6 field-dependent magnetization was recorded. A second field-dependent magnetization was
7 recorded after having cooled down to 5 K (-268 °C) while the 5 T magnetic field was applied.

8 Temperature-programmed reduction (TPR) profiles of the calcined catalysts were recorded
9 with a Micromeritics AutoChem 2920 Analyzer in the temperature range of 50-1000 °C, in
10 order to determine the reducible species present in the catalyst and to reveal the temperature at
11 which the reduction occurs. 100 mg of the sample was placed in a quartz reactor and reduced
12 by a 5% H_2/N_2 gas mixture with a flow rate of 25 mL.min⁻¹ and a heating rate of 10 °C.min⁻¹.
13 Prior to the analysis, the samples were purged under argon at 120 °C for 1 h.

14 The cobalt loading of the catalysts was determined by inductively coupled plasma optical
15 emission spectrometry (ICP-OES) after mineralization of the samples in a mixture of
16 HNO_3/HCl at 190 °C in an inert autoclave for one day.

17 Hydrogen temperature programmed desorption coupled with mass spectroscopy (H_2 -TPD-MS)
18 (Altamira Instruments AMI-300 device) was used in order to characterize the nature of oxygen
19 surface groups after HNO_3 treatment, to elucidate the nature of hydrogen species during the
20 desorption step, and to determine the average active particle size of metal in supported Co-
21 catalysts. First, the catalyst was purged with argon at 120 °C for 1 hour in order to clean the
22 surface of the sample. Then, the system was cooled to 50 °C followed by a reduction at 350 °C
23 for 6 h at 5 °C.min⁻¹ under 5% H_2/N_2 flow and then cooled down to 100 °C under hydrogen
24 flow. The H_2 chemisorption took place at 100 °C. Then the flow of hydrogen was switched to

1 helium until 50 °C. H₂-TPD-MS was finally performed (10 °C.min⁻¹ ramp until 1050 °C) to
2 quantify the amounts of released H₂, CO, and CO₂. The H₂ peak surface (400-800 °C) was used
3 to determine the cobalt dispersion (Eq. 5) and average particle size (Eq. 6) by the following
4 formula:

$$5 \quad D(\%) = \frac{V_m \times M \times F}{V_{mol} \times \%Me} \times 100 \quad (Eq. 5)$$

6 Where V_m is the irreversibly chemisorbed gas (cm³, STP per gram of catalyst), M is the molar
7 mass of the metal (g per mol of metal), V_{mol} is the standard molar volume of the adsorbate (cm³
8 STP per mol), % Me is the mass fraction of metal, and F is the stoichiometry factor (number of
9 gas molecules per atom of metal) [20].

$$10 \quad d_{Co}(\text{nm}) = \frac{96}{D\%} \quad (Eq. 6)$$

11 Where d_{Co} (nm) is the average particle size.

12 **2.3 Fischer Tropsch synthesis**

13 FT synthesis was performed in a fixed-bed reactor composed of a stainless-steel tube of 33 cm
14 length and 14 mm inner diameter. The reactor was loaded with 36 g of α-Al₂O₃ followed by a
15 mixture of 2 g of catalyst and 8 g of inert SiC (125-250 μm) in order to well dissipate the heat
16 released from the reaction, and finally 20 g α-Al₂O₃ and a quartz wool layer. A thermocouple
17 was placed at the center of the catalyst bed to control the reaction temperature. The reactor was
18 heated from ambient temperature to 120 °C with a heating rate of 1 °C.min⁻¹ under a flow of
19 argon (100 mL.min⁻¹) for 1 hour. Then, the catalyst was reduced *in situ* under a 40%H₂/Ar (100
20 mL.min⁻¹) flow at 350 °C for 8h with a heating rate of 5 °C.min⁻¹. After the reduction, the FT
21 reaction was carried out at 220 °C and 20 bar for 94 h. The inlet gas mixture was composed of
22 52% (v/v) H₂, 25% (v/v) CO and 23% (v/v) Ar. The condensable products were recovered using
23 a hot condenser (150 °C) followed by a cold condenser (4 °C) and analyzed by GC-SIMDIST

1 (SHIMAZU) equipped with a flame ionization detector (FID). The non-condensable gaseous
2 products recovered after the cold condenser were analyzed by μ -GC (A 3000 model, Agilent)
3 equipped with a thermal conductivity detector (TCD). The catalytic tests were repeated twice.
4 The catalytic performances were calculated using the following equations:

5 CO conversion (X_{CO} , %, Eq. 7):

$$6 \quad X_{CO} = \frac{\dot{F}_{CO,i} - \dot{F}_{CO,out}}{\dot{F}_{CO,i}} \quad (\text{Eq.7})$$

7 Where: $\dot{F}_{CO,i}$ = molar flow rate [$\text{mol}\cdot\text{s}^{-1}$] of CO fed to the reactor ($\text{mol}\cdot\text{s}^{-1}$); $\dot{F}_{CO,out}$ = molar
8 flow rate [$\text{mol}\cdot\text{s}^{-1}$] of CO at the reactor outlet ($\text{mol}\cdot\text{s}^{-1}$)

9 CTY = Cobalt-Time-Yield ($\text{mol}_{CO}\cdot\text{mol}_{Co}^{-1}\cdot\text{s}^{-1}$, Eq. 8):

$$10 \quad \text{CTY} = \frac{\dot{F}_{CO,i} \times X_{CO} \times M_{Co}}{m_{cat}} \quad (\text{Eq.8})$$

11 Where: $\dot{F}_{CO,i}$ = molar flow rate [$\text{mol}\cdot\text{s}^{-1}$] of CO fed to the reactor ($\text{mol}\cdot\text{s}^{-1}$); m_{cat} = mass of
12 catalyst (g); M_{Co} = molar mass of Co ($\text{g}\cdot\text{mol}^{-1}$).

13 Turn-over frequency (TOF, s^{-1} , Eq. 9):

$$14 \quad \text{TOF} = \frac{\text{CTY} \times M_{Co}}{D_{Co} \times x_{Co}} \quad (\text{Eq.9})$$

15 Where: x_{Co} = Co loading ($\text{g}_{Co}\cdot\text{g}_{cat}^{-1}$); D_{Co} = Co dispersion calculated based on the TEM Co size
16 after the catalytic tests.

17 Selectivity into a given hydrocarbon j containing i carbon atoms (S_i , %, Eq. 10):

$$18 \quad S_i = \frac{i \times \dot{F}_j}{\dot{F}_{CO,i} - \dot{F}_{CO,out}} \times 100 \quad (\text{Eq.10})$$

1 Where: S_i = selectivity; \dot{F}_j = molar flow rate of the corresponding product quantified at the
2 reactor outlet [21].

3 **3. Results and discussion**

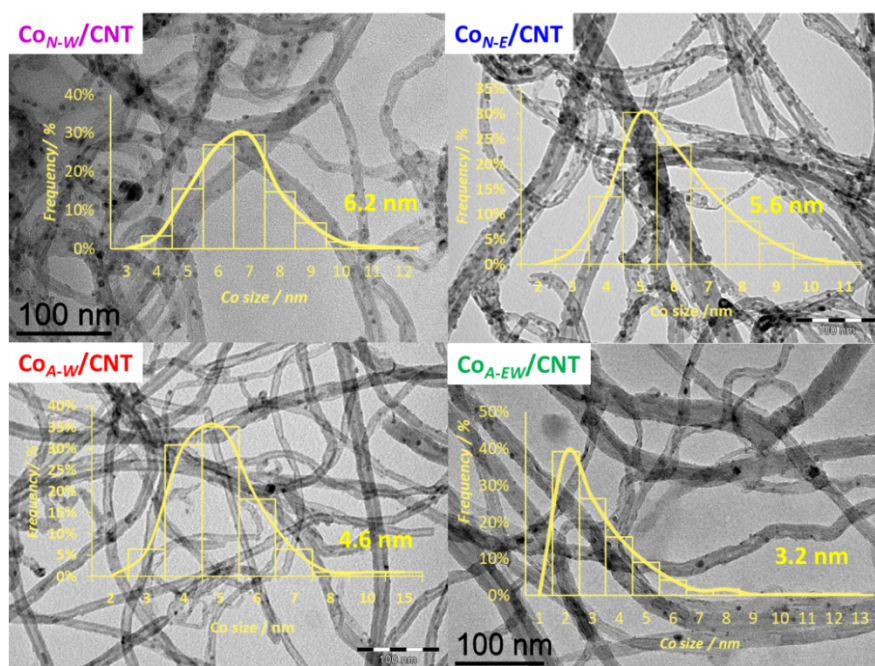
4 **3.1 Catalyst characterization and influence of the support on catalyst features**

5 Nitric acid oxidized CNT ($220 \text{ m}^2 \cdot \text{g}^{-1}$, $d_{ext.} = 12.6 \text{ nm}$ and $d_{int.} = 4.5 \text{ nm}$) were used to support
6 the cobalt active phase. The chemical and textural properties of this carbon support are given
7 in Table S1. IWI was performed to load 15% Co *w/w* in water or ethanol for the nitrate precursor
8 yielding $\text{Co}_{N-W}/\text{CNT}$ and $\text{Co}_{N-E}/\text{CNT}$ catalysts, respectively. For the acetate precursor (same
9 metal loading), the IWI was performed in water and ethanol/water mixtures (for solubility
10 reasons), yielding $\text{Co}_{A-W}/\text{CNT}$ and $\text{Co}_{A-EW}/\text{CNT}$ catalysts, respectively. ICP-OES analyses of
11 the calcined catalysts (Table 1) showed cobalt loadings of 17.8 ($\text{Co}_{N-W}/\text{CNT}$), 16.0 ($\text{Co}_{N-E}/\text{CNT}$),
12 16.0 ($\text{Co}_{A-W}/\text{CNT}$), and 17.5 wt% ($\text{Co}_{A-EW}/\text{CNT}$). Catalyst characterization was performed on
13 calcined, freshly reduced ($350 \text{ }^\circ\text{C}$) and spent catalysts. First, we focused on the size of the cobalt
14 particles, their possible confinement, their crystallographic phase (*hcp/fcc*), and their reduction
15 degree ($\text{Co}^0/\text{Co}^{n+}$). Then, we have assessed the influence of CNT surface chemistry and H_2
16 spillover. Finally, the catalytic performances were correlated to catalyst properties (Co particle
17 size, reducibility, phase, confinement and hydrogen spillover).

18 ***Cobalt particle size, confinement, crystallographic phase and composition.***

19 The mean cobalt particle size of the reduced catalyst after exposure to air was estimated by
20 TEM (Fig. 1) and XRD line broadening analysis (Fig. S2, Table 1). The TEM analyses show
21 relatively small cobalt particles of 3-6 nm with smaller particles obtained for the acetate
22 precursor for a given solvent, and in ethanol for a given precursor. The Co mean particle size
23 follows the order $\text{Co}_{N-W}/\text{CNT}$ (6.2 nm) > $\text{Co}_{N-E}/\text{CNT}$ (5.6 nm) > $\text{Co}_{A-W}/\text{CNT}$ (4.6 nm) > Co_{A-}
24 EW/CNT (3.2 nm). In addition, HRTEM observations show that a significant number of Co

1 particles are confined in the inner cavity of CNT (Fig. S3 and Table 1), particularly in the case
2 of the *ex-nitrate* catalysts.



3
4 **Figure 1.** TEM micrographs and Co particle size distribution of the four catalysts.

5
6 Whatever the catalyst, the Co mean particle size is smaller for the confined particles than for
7 those deposited on the external surface (Fig. S4). The filling yield, calculated according to a
8 simple relation [16], follows the order Co_{N-E}/CNT 5.6 nm (74 %) > Co_{N-W}/CNT 6.2 nm (57 %)
9 > Co_{A-W}/CNT 4.6 nm (27 %) > Co_{A-EW}/CNT 3.2 nm (16 %). Cobalt filling yields of 10-30%
10 have been previously reported for highly loaded Co/CNT catalysts (10-15% w/w) prepared
11 from cobalt nitrate on HNO₃ oxidized open-ended CNT [12,22]. For the cobalt acetate
12 precursor, a small portion of particles was reported to be encapsulated in Co_A/CNT catalysts
13 [23], but the amount has not been quantified. The lower filling yield and higher dispersion
14 obtained for the *ex-acetate* catalysts could be related to the ability of acetate ions to deprotonate
15 surface -OH groups [24,25] (phenolic or carboxylic in the case of CNT) with concomitant

1 acetic acid formation and thus to favor cobalt grafting and dispersion on the newly created
2 surface groups on the external surface of CNT.

3 The smaller Co mean particle size (for both *ex-nitrate* and *ex-acetate* catalysts), and the higher
4 filling yield (for *ex-nitrate* catalyst) obtained in ethanol can be rationalized by solvent surface
5 tension considerations. Indeed, higher filling yield [16,26], and better metal dispersion
6 (controlled during the drying step) [14] for CNT-supported metal catalysts were reported for
7 solvents showing low surface tension. The ethanol surface tension at 20 °C is 22.4 mN.m⁻¹,
8 whereas the one of water is 72.8 mN.m⁻¹. The isotherms of ethanol and water adsorption and
9 desorption on CNT are shown in Fig. S5. The hydrophobic character of the CNT surface and
10 the high polarity of the water molecules induces a shift in water adsorption towards higher
11 relative pressures compared to ethanol vapors. The large hysteresis observed on the water
12 isotherms can be tentatively correlated with the presence of an open CNT inner cavity.
13 Comparing the adsorption of water and ethanol vapors on CNT, the initial relative pressure of
14 the isotherm depends on the polarity of the adsorbents; and at low pressures, the adsorption of
15 ethanol on CNT is higher than that of water. These results demonstrate that the exploitation and
16 interpretation of impregnating solvent adsorption isotherms by measuring surface tensions is
17 an interesting discriminant analysis to not only to rationalize the results obtained in terms of
18 filling yield and metal dispersion, but also guide the choice of impregnation solvent for IWI.
19 Here, the use of ethanol, a solvent with low surface tension, allows a better wetting of the CNT
20 surface, and results in higher filling yield and cobalt dispersion.

21 Figure S2 shows the *ex-situ* X-ray diffraction patterns of the catalysts after reduction at 350 °C
22 for 2 hours and exposure to air. The two peaks observed on the XRD pattern at 30 and 51°
23 correspond to the (002) and (100) reflection planes of CNT. Peaks corresponding to Co_{hcp}, Co_{fcc},
24 CoO and Co₃O₄ were present for all four catalysts. The calculation of the average size of
25 crystallites from the Scherrer equation, and using the peak at 42° or 36°, which corresponds to

1 the Co_3O_4 phase, was made by using the relation $d(\text{Co}^0) = 0.75 \times d(\text{Co}_3\text{O}_4)$ [17]. The mean
2 XRD particle size was in very good agreement with the one determined by TEM (Table 1).

3 The evolution of the Co crystallographic phases was monitored by *in-situ* XRD during the
4 reduction of the calcined catalysts (Figure 2). At 30 °C, all catalysts show the presence of the
5 CoO and Co_3O_4 phases. The presence of small amounts of CoO could be attributed to the auto-
6 reduction of Co_3O_4 assisted by CO evolved from the decomposition of the support functional
7 groups during the calcination step [27]. Co_3O_4 is fully reduced to CoO at 300-450 °C. Then,
8 CoO reduction progressively took place from 300 to 550 °C to form Co_{hcp} and Co_{fcc} . The carbon
9 peak at $2\theta = 30^\circ$ significantly decreased at 700-800 °C due to cobalt-catalyzed carbon
10 hydrogasification [28]. This phenomenon is more pronounced for the $\text{Co}_{A-W}/\text{CNT}$ and
11 particularly for $\text{Co}_{A-EW}/\text{CNT}$ catalysts, due to their higher cobalt dispersion.

12 Figure 2 also shows the quantitative evolution of the crystalline phases as a function of
13 temperature. The reduction degree and the $\text{Co}_{hcp}/\text{Co}_{fcc}$ ratio (Fig. S6) were determined at 350
14 °C, which corresponds to the *in-situ* reduction temperature before the FTS tests. **As the *in-situ***
15 **XRD experiments were performed with an isotherm of 22 min at 350 °C, we independently**
16 **checked that the XRD diagrams (Fig. S7 and Table S2) did not evolve upon a prolongation of**
17 **the isotherm to 8 h (as performed *in-situ* before the FTS tests).** The degree of reduction follows
18 the order: $\text{Co}_{A-W}/\text{CNT}$ (88 %) > $\text{Co}_{A-EW}/\text{CNT}$ (83 %) > $\text{Co}_{N-W}/\text{CNT}$ (67 %) > $\text{Co}_{N-E}/\text{CNT}$ (49 %);
19 and the $\text{Co}_{hcp}/\text{Co}_{fcc}$ ratio follow the order: $\text{Co}_{N-W}/\text{CNT}$ (8.28) > $\text{Co}_{N-E}/\text{CNT}$ (5.12) > $\text{Co}_{A-W}/\text{CNT}$
20 (1.93) > $\text{Co}_{A-EW}/\text{CNT}$ (0.69). The differences observed in the reduction degree and the
21 $\text{Co}_{hcp}/\text{Co}_{fcc}$ ratio can be rationalized by differences in the CNT surface chemistry of the different
22 samples (*vide infra Effect of carbon surface chemistry on catalyst features and hydrogen*
23 *spillover*). **Since XRD cannot detect eventual very small particles/clusters, we also performed**
24 **STEM/HAADF analyses on $\text{Co}_{A-W}/\text{CNT}$ and $\text{Co}_{A-EW}/\text{CNT}$ samples (Fig. S8). These analyses**
25 **confirm the absence of such species on the investigated catalysts.**

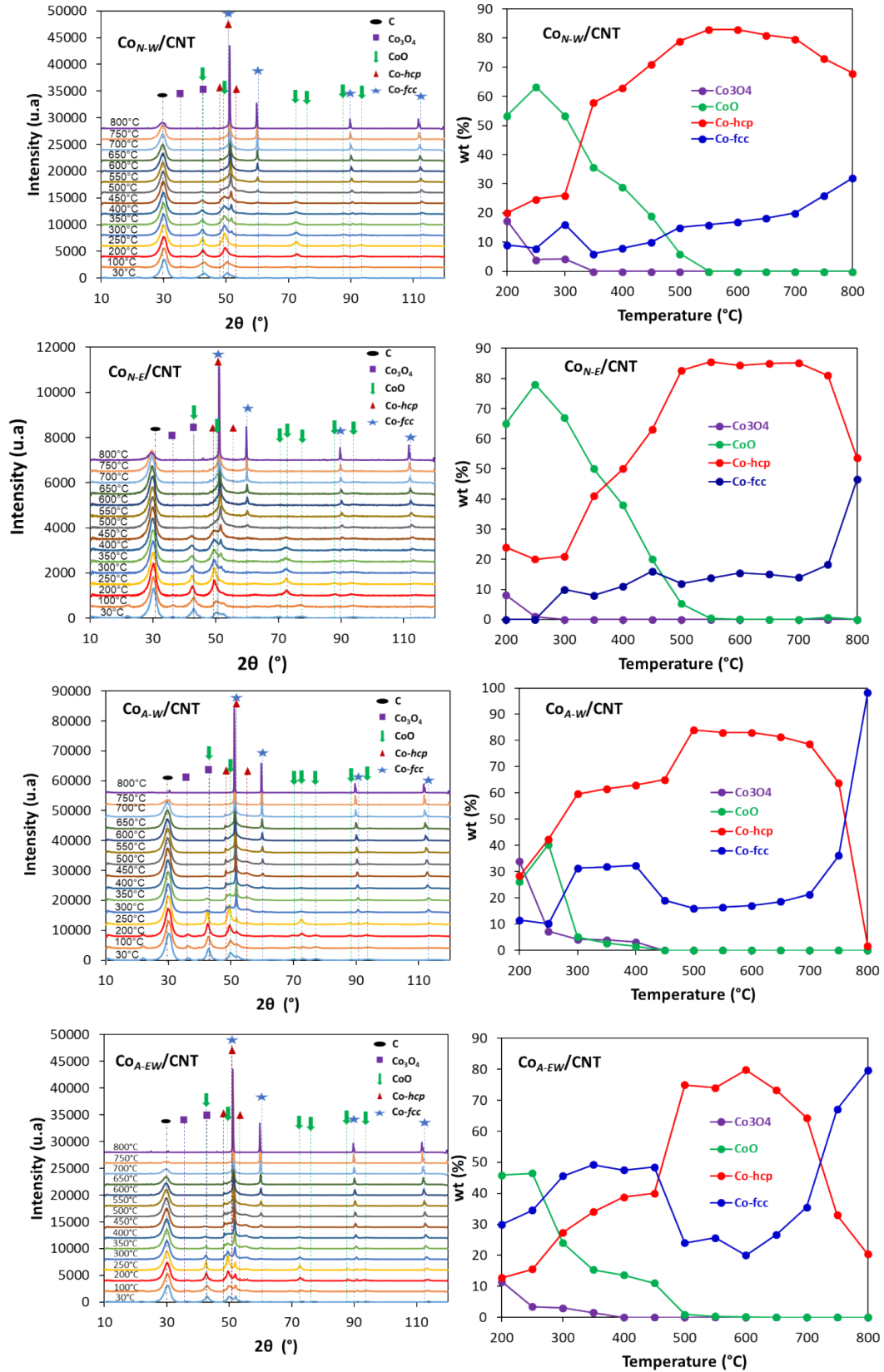


Figure 2. XRD patterns and evolution of the Co crystal phases during the *in-situ* reduction under 5% H_2/N_2 flow from 30 to 800 °C (temperature ramp $5^\circ\text{C}\cdot\text{min}^{-1}$).

1 The reduction degree of Co catalysts can also be determined by magnetometry at room
2 temperature [29]. CoO being non-magnetic it does not contribute to the magnetization of the
3 sample. Thus, a decrease in the M_s as compared to the bulk Co magnetization value (163
4 $\text{emu.g}_{\text{Co}}^{-1}$) [30] means that part of the Co present in the sample is oxidized. The total Co in the
5 sample being known from ICP, the CoO amount can be calculated. Therefore, the reduction
6 degree of the catalysts after reduction in 40% H_2 /Ar flow for 8 h at 350 $^\circ\text{C min}^{-1}$ was determined
7 by magnetic measurements without exposing the samples to the air. The sample magnetization
8 versus the intensity of the applied magnetic field was recorded at 300 K (Fig. S9 and Table 1).

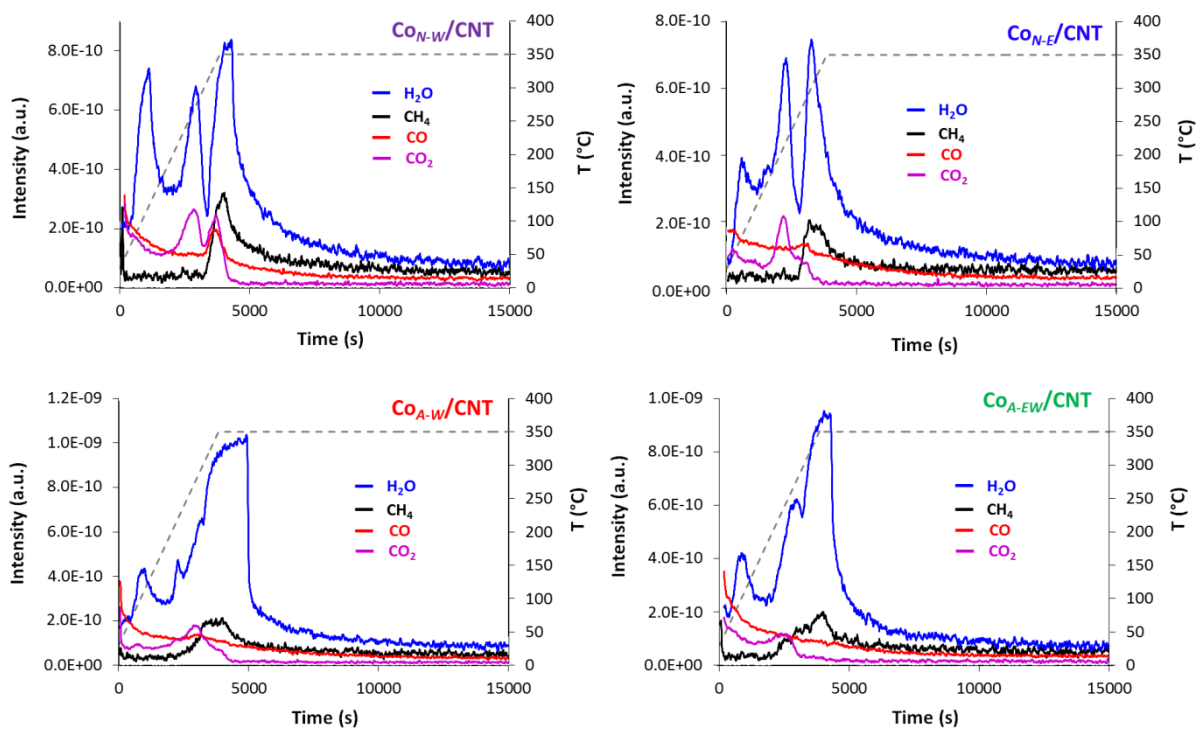
9 The magnetizations at saturation (M_s) of $\text{Co}_{N-W}/\text{CNT}$, $\text{Co}_{N-E}/\text{CNT}$, $\text{Co}_{A-W}/\text{CNT}$ and $\text{Co}_{A-EW}/\text{CNT}$
10 catalysts are 121, 60, 135.5 and 129.7 $\text{emu.g}_{\text{Co}}^{-1}$, respectively. From these values, and
11 considering the magnetization of bulk Co, the reduction degree of the studied catalysts was
12 determined to be 76% for $\text{Co}_{N-W}/\text{CNT}$, 37% for $\text{Co}_{N-E}/\text{CNT}$, 85% for $\text{Co}_{A-W}/\text{CNT}$ and 81% for
13 $\text{Co}_{A-EW}/\text{CNT}$. These values are in good agreement with the *in-situ* XRD data (Table 1). The
14 reducibility of the catalysts was studied by temperature-programmed reduction. Figure S10
15 shows the TPR profiles of the calcined catalysts. Three broad peaks are observed at 250-320
16 $^\circ\text{C}$ (I), 370-460 $^\circ\text{C}$ (II) and 550 $^\circ\text{C}$ (III). The two first peaks (I and II) correspond to the typical
17 two-step reduction of cobalt catalysts, from Co_3O_4 to CoO, then CoO to metallic cobalt. The
18 last peak (III) is attributed to the catalytic gasification of the carbon support [12]. The
19 decomposition of CNT surface oxygen groups (accompanied by CO or CO_2 release), and further
20 reduction by H_2 of carbon oxides to methane over Co particles, which is also possible in this
21 temperature range [31]. A complete reduction of Co_3O_4 consumes one hydrogen molecule for
22 the first reduction process ($\text{Co}_3\text{O}_4 + \text{H}_2 \rightarrow 3\text{CoO} + \text{H}_2\text{O}$), and three hydrogen molecules for the
23 second ($3\text{CoO} + 3\text{H}_2 \rightarrow 3\text{Co} + 3\text{H}_2\text{O}$). It is thus expected that the reduction peak areas of Co_3O_4
24 to CoO and CoO to Co will have a ratio of 1:3. As expected from the *in-situ* XRD experiments,
25 the position of peak (I) is shifted to lower temperatures for the two *ex-nitrate* catalysts (260-290

1 °C), which fits well with the data reported in the literature (220-280 °C) [32,33]. The lower
2 reduction temperature observed for the first peak of the *ex*-nitrate catalysts could be explained
3 by a confinement effect [22,34]. Considering the width of peaks II and III, it seems hazardous
4 to comment on the differences observed in Figure S10 between the four profiles. However,
5 neither *in-situ* XRD nor these TPR experiments point to an easier complete reduction of the *ex*-
6 nitrate catalysts compared to the *ex*-acetate ones, which could be in part due to a possible
7 confinement effect [34], even if the absence of confinement effects on the reduction temperature
8 of Co/CNT catalysts has been reported [35]. It is also worth noting the smaller cobalt particles
9 present on the Co_{A-W}/CNT and Co_{A-EW}/CNT catalysts that are the first to be completely reduced
10 (Fig. 2). Thus, besides confinement effects, the Co particle size and the strength of the MSI
11 should also be considered to rationalize the easier reduction (and reduction degree) of the *ex*-
12 acetate catalysts (*vide infra*).

13 For FTS tests, the catalysts were reduced at 350 °C for 8 h under an H₂/Ar atmosphere. We
14 followed this reduction by TPD/MS analyses (350 °C, H₂/N₂, 6 h) to probe the nature of the
15 evolved gases (Fig. 3). The analysis of these spectra is very informative about the complex
16 surface chemistry that takes place during the reduction of the catalyst. First, the amount of water
17 evolved is significantly higher for the *ex*-acetate catalysts, in accordance with the higher
18 reduction degree determined by *in-situ* XRD and VSM experiments. Water evolution occurs in
19 three steps: at 100-150 °C, at 220-270 °C, and at 300-350 °C. The first peak that corresponds
20 to the desorption of physisorbed water is logically more intense for the Co_{N-W}/CNT, which has
21 been prepared in water. This catalyst also presents a larger peak area of CO+CO₂ releasing
22 groups (Table S3). The second peak at 220-270 °C should be mainly associated to the reduction
23 of Co₃O₄ to CoO. Additionally, in this temperature range, CO₂ evolution also occurs by the
24 catalytic decomposition of the carboxylic groups of the support (*vide infra* Fig. 4a), which can
25 also produce water [36]. Finally, the more intense last peak (300-350 °C) is associated with the

1 reduction of CoO to Co⁰. In this temperature range, the evolution of CO₂/CO is also observed
2 (Fig. 3), which should in principle arise from the catalytic decomposition of carboxylic
3 anhydrides [37], with the concomitant formation of methane. The formation of methane in this
4 temperature range should be associated to the CO methanation activity of the cobalt phase,
5 which also produces water [38,39].

6



7

8 **Figure 3.** TPD-MS spectra of H₂O, CH₄, CO and CO₂ obtained during the catalyst reduction
9 step.

10

Table 1. Summary of the results of catalyst characterization and catalyst activity in FTS.

Catalyst	^{a)} Co (%)	d_{TEM} (nm)	d_{XRD} (nm)	Co_{hcp}/Co_{fcc}	Reduction degree		Co filling yield (%)
					<i>in-situ</i> XRD (%)	VSM	
Co _{N-W} /CNT	17.8	6.2	7.3	8.3	67	75	57
Co _{N-E} /CNT	16	5.6	5.8	5.1	49	36	74
Co _{A-W} /CNT	16	4.6	4.1	1.9	88	83	27
Co _{A-EW} /CNT	17.5	3.2	3.3	0.7	83	80	16

^{a)} From ICP analyses.

XPS analyses were performed in order to probe the MSI. Figure S11 shows the Co 2p spectra normalized on the C 1s peak for the four calcined catalysts after air exposure. The Co/C atomic ratio (Table 2) is higher for the *ex*-acetate catalysts, which contain lower number of confined nanoparticles and present smaller mean particle sizes than those of *ex*-nitrate catalysts. Distinct peaks (Table 2) stemming from 2p_{3/2} at 779.5-781.1 eV and 2p_{1/2} at 794.7-796.8 eV can be seen, characteristic of Co²⁺ and Co³⁺ species. The Co 2p spectra were deconvoluted into several components. The synthetic components in Co 2p_{3/2} spectra at 779.5-779.8, and 781.0-781.3 eV can be assigned, respectively, to CoO and Co₃O₄. The Co³⁺/(Co²⁺+Co³⁺) ratio does not change significantly between the different samples (~ 0.5), and the data obtained by XPS are consistent with those obtained by XRD on these same calcined samples (not shown), for which the ratio was also around 0.5.

Table 2. Co/C atomic ratio, Co³⁺/(Co²⁺+Co³⁺) ratio, and Co 2p binding energy (BE) of the catalysts.

Catalyst	Co/C	Co ³⁺ /(Co ²⁺ +Co ³⁺)	Co binding energy (eV)			
			2p _{3/2}		2p _{1/2}	
			Co ³⁺	Co ²⁺	Co ³⁺	Co ²⁺
Co _{N-W} /CNT	0.03	0.43	779.8	781.3	795.0	796.8
Co _{N-E} /CNT	0.02	0.49	779.7	781.1	795.0	796.9
Co _{A-W} /CNT	0.03	0.49	779.5	781.0	794.7	796.2
Co _{A-EW} /CNT	0.04	0.47	779.6	781.0	794.7	796.3

For the *ex*-nitrate catalysts, both 2p_{1/2} and 2p_{3/2} peaks are shifted to higher binding energies, 779.7/779.8 and 795.0 eV, respectively, compared to the *ex*-acetate catalysts (779.5/779.6 and 794.7 eV). These shifts reveal that the strength of the interaction between oxidized Co species and CNT varies across the catalyst series. The *ex*-nitrate catalysts, even if they present a larger particle size, present a stronger interaction with the supports, which can explain their lower degree of reduction (*vide supra*).

In order to obtain further information on the reason of these different interactions, which lead to differences in the reducibility of cobalt, and in order to explain the different $\text{Co}_{hcp}/\text{Co}_{fcc}$ ratios observed, the surface chemistry of the support was examined.

Effect of carbon surface chemistry on catalyst features and hydrogen spillover

The surface chemistry of the carbon support can influence the final features of the supported catalyst in a number of ways [40,41]. Indeed, metal dispersion [42,43], MSI [44,45], metal location [16,46], and H-spillover [9,47] have been reported to be influenced by the surface chemistry of the carbon support. The carbon surface being rather inert, it is generally accepted that it is necessary to functionalize it in order to disperse and stabilize the metallic phase [48]. Nevertheless, questions exist on the stability of the functional surface groups during catalyst preparation, and particularly during the calcination and reduction steps, generally carried out at high temperatures. The chemistry that can take place during these key steps of catalyst preparation between the metal precursor and the support surface is crucial for the determination of catalyst properties, complex and most of the times insufficiently discussed.

The thermal decomposition of cobalt acetate under an inert atmosphere has been studied *via* thermogravimetric analysis, *in-situ* XRD, and FTIR [49]. The volatile products formed during the decomposition are water vapor, acetic acid, ethenone (ketene), acetone, and CO_2 . In the case of cobalt nitrate decomposition under an inert atmosphere, water vapor and various nitrogen oxides (NO , NO_2 , N_2O_4 and N_2O_5) are the produced volatile products [50]. In our study, TGA analyses were performed with the dried $\text{Co}_{N-W}/\text{CNT}$ and $\text{Co}_{A-W}/\text{CNT}$ catalysts under N_2 (Figure S12). The temperature program was the same as the one followed for catalyst calcination (N_2 , 20 °C to 350 °C at 10 °C.min⁻¹ followed by an isotherm of 3 h at 350 °C). The reaction starts at lower temperature for the $\text{Co}_{N-W}/\text{CNT}$ catalyst and finishes faster for the $\text{Co}_{A-W}/\text{CNT}$ catalyst. The weight losses of the two samples are very different. It is only 3.3 % for $\text{Co}_{A-W}/\text{CNT}$ and 22.1 % for $\text{Co}_{N-W}/\text{CNT}$. The low weight loss observed for the $\text{Co}_{A-W}/\text{CNT}$ catalyst could be

explained by the loss of acetic acid (formed by deprotonation of surface –OH groups by acetate ions) during the impregnation or drying steps. Another explanation could be a reaction between the decomposition products and the carbon surface leading to its functionalization. The important weight loss observed for the Co_{N-W}/CNT catalyst (resulting mainly from nitrogen oxide) can have a pronounced influence on the CNT surface chemistry. Indeed, it is known that the (catalyzed) oxidation of carbon by NO_x can contribute to the formation of oxygen functional groups and even to carbon gasification [51–53].

TPD-MS analysis is a common method for the characterization of the oxygen-containing surface groups of carbon materials, which decompose releasing CO and/or CO₂ and in some cases H₂O at different temperatures (Table S4) [37,41]. The evolution of CO₂, CO and H₂ during TPD-MS analyses under helium for the four reduced catalysts provide valuable information on Co reducibility, Co crystal phase and H₂ spillover, respectively, and they are shown on Figure 4. The analyses were performed after the *in-situ* reduction of the calcined catalysts under the same conditions than the ones used during the FTS tests (20 °C to 350 °C at 10°C.min⁻¹ under inert/H₂ mixture followed by an isotherm of 6 h. at 350 °C, Figure 3) to probe the surface chemistry. It is worth pointing out that nitro groups decompose at about 280 °C, resulting in the release of NO₂ [54]; thus, such groups are not present on the catalyst surface. Looking at the CO₂ and CO spectra, it is clear that the catalyst surface chemistry drastically changes during catalyst preparation. The CNT support contains carboxylic (CO₂ at 217/291 °C), carboxylic anhydride (CO₂ and CO at 437 °C), lactone (CO₂ at 576 °C), phenol (CO at 717 °C) and carbonyl/quinone (CO at 882 °C) surface groups (see Tables S5 for the results of the deconvolution of CO₂ and CO profiles of CNT using a multiple Gaussian function).

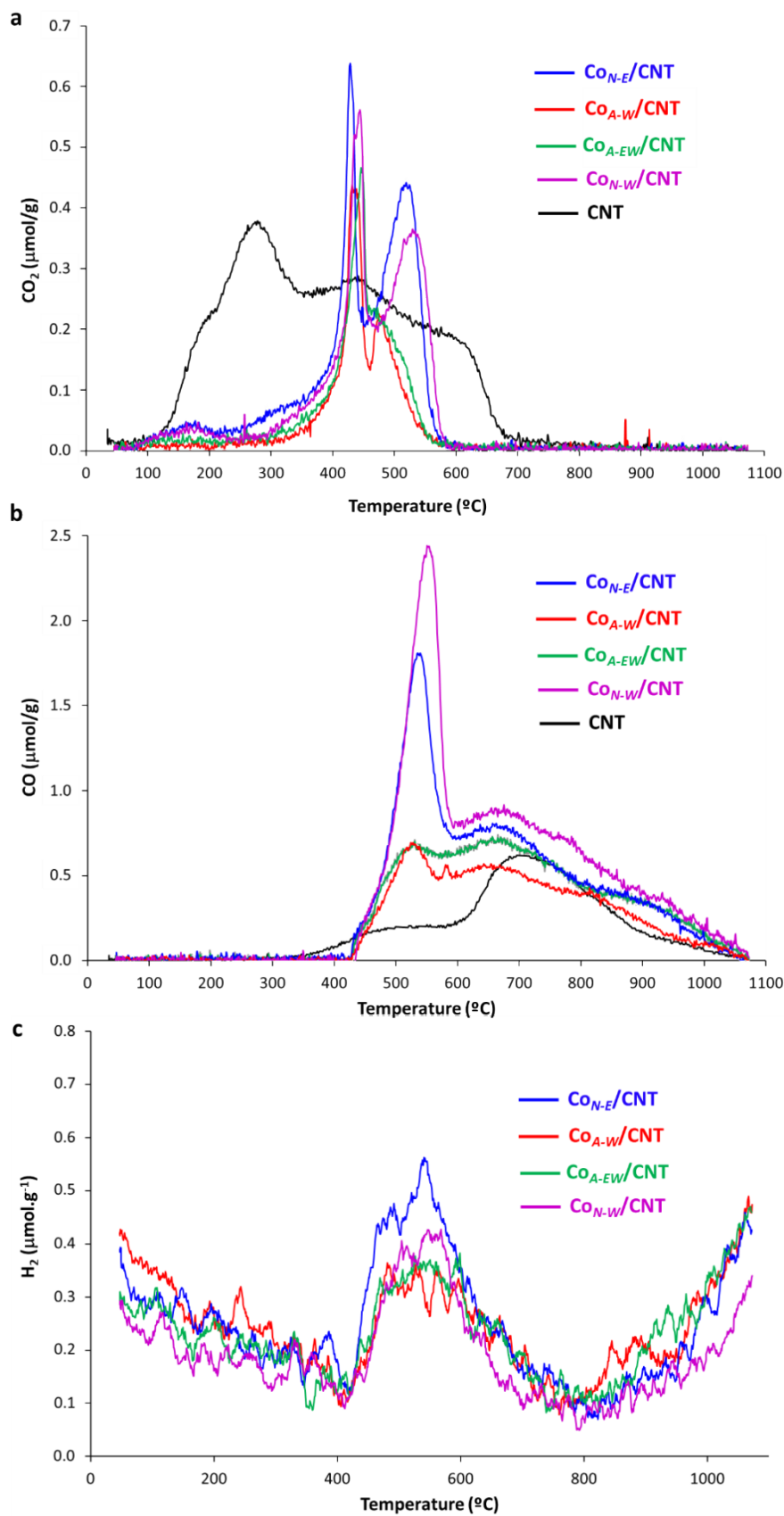


Figure 4. TPD/MS spectra of the catalysts and CNT support: a) CO₂ evolution; b) CO evolution; and c) H₂ evolution.

As expected, considering their decomposition temperature, the carboxylic groups (Figure 4a) disappear almost completely upon catalyst preparation at 350 °C, and a Co(OOC-) interface is created for the four catalysts, associated to a narrow and intense peak characteristic of a catalytic decomposition between 427 and 448 °C, depending on the catalyst. This phenomenon has already been reported for Ru/CNT [55] and Pd/CNT [56] catalysts prepared on oxidized CNT. It is also obvious from Figure 4a,b that new functionalities are created on the *ex*-nitrate catalysts associated to a significant CO₂ evolution at 515-530 °C and a CO evolution at 530-555 °C. The appearance of these new surface groups during catalyst preparation and their influence on catalyst properties are discussed below.

CO₂ releasing groups on catalyst surface and their influence on cobalt reducibility.

The CO₂-releasing groups on the catalyst surface (Figure 4a, and Figure S13 and Tables S3 for CO₂ deconvolution profiles of the Co/CNT catalysts) are of three main types: i) residual carboxylic groups decomposing at ~160 (peak#1) and ~380-420 °C (peak#2); ii) Co(OOC-) interface groups (peak#3) decomposing at ~440 °C; and iii) groups decomposing at ~450-490 (peak#4) and ~490-530 °C (peak#5). This third type of groups is particularly present for the *ex*-nitrate catalysts. They could be created by (catalyzed) oxidation with nitrogen oxides, and considering the narrow peaks, they most likely decompose catalytically over a temperature range, which could correspond to carboxylic anhydrides or lactones. The decomposition of carboxylic anhydride also produces CO, and CO is indeed produced (Figure 4b and Figure S14) at similar temperatures (450-460 °C). In addition to carboxylic acids, carboxylic anhydrides and lactones have been reported to form during carbon oxidation with gaseous nitric acid (a complex mixture of HNO₃, O₂, H₂O, and various nitrogen oxides) [57,58]. Since in our case, the formation/decomposition of these groups can be cobalt-assisted, it is difficult to make a rigorous assignment. Nevertheless, considering their decomposition temperature, we propose that peak#4 corresponds to anhydrides, possibly coordinated to cobalt, and peak#5 corresponds

to lactone surface groups. The peak#3 associated to the cobalt-support interface (Co(OOC-) species) can be related to the strength of the MSI, and consequently to cobalt reducibility. On CNT-supported catalysts, it has been reported that the presence of lateral surface-carboxylate ligands on metallic particles significantly contributes to strengthen the MSI [55]. It is clear from Figure 5a that the cobalt-surface carboxylate interface is more developed for the *ex*-nitrate catalysts than for the *ex*-acetate ones, even if these latter present a smaller Co mean particle size. It is thus reasonable to propose that the Co particles of the *ex*-nitrate catalysts should interact stronger and should be more difficult to reduce than the ones of the *ex*-acetate catalysts. In fact, a very good correlation was found between the concentration of the Co(OOC-) species (Tables S3) and the reduction degree of the catalysts (Figure 5a). The cobalt nitrate decomposition during the impregnation/calcination step contributes to CNT oxidation, and to the creation of a strong MSI, limiting further cobalt reduction. Thus, the chemical reactions taking place (or not) between the metal precursor and the carbon support during catalyst preparation can affect the MSI.

CO releasing groups on catalyst surface and their influence on the produced cobalt phase.

The CO-releasing groups on the catalyst surface (Figure 4b and Figure S13 and Tables S3) are of five types: i) the carboxylic anhydrides, which are the less abundant decomposing at ~510-540 °C (peak#1); ii) phenol groups decomposing at ~525-550 °C (peak#2), iii) ether groups decomposing at ~650-680 °C (peak#3) [59], iv) carbonyl/quinone groups decomposing at ~800-820 °C (peak#4), and v) low amount of groups decomposing at ~930-950 °C (peak#5) that could correspond to chromene or pyrone [60–62]. The decomposition of the cobalt nitrate precursor during catalyst preparation induces the formation of large amounts of phenolic groups, starting releasing CO at around 450 °C. These groups could be formed directly, or by catalytic reduction (either on cobalt particles or *via* the H-spillover) of transient carboxylic/anhydride groups (Figure 3) [63].

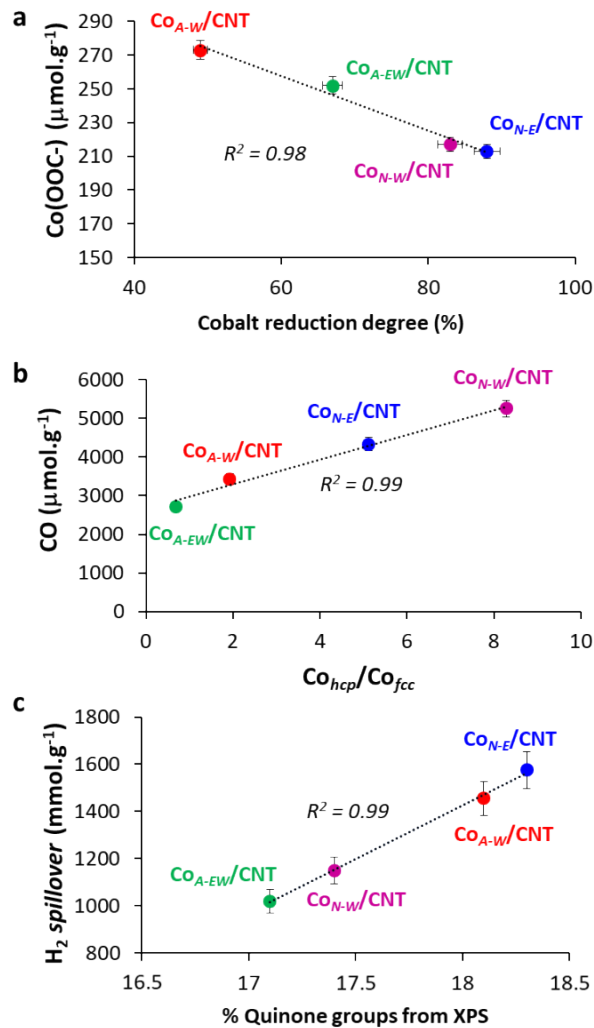


Figure 5. Correlation between: a) the cobalt reduction degree and the amount of CO₂ evolved from the Co(OOC-) interface; b) the Co_{hcp}/Co_{fcc} ratio and the amount of CO evolved from the catalyst support; and c) the percentage of quinone groups on the catalyst support and the total amount of H₂ desorbed from spillover.

The formation of phenol groups has been reported to occur during the impregnation/drying steps of nitrate salts on activated carbon [64]. The release of CO even during the reduction step of the catalyst at 350 °C (Figure 3) is interesting. It is known that the presence of CO during the reduction of cobalt FTS catalysts can favor the formation of Co_{hcp} through the transient formation and decomposition of cobalt carbide (Co₂C) [65–67]. Indeed, the *in-situ* XRD

experiments ($5\text{ }^{\circ}\text{C}\cdot\text{min}^{-1}$ from 30 to $800\text{ }^{\circ}\text{C}$ with plateau of 22 min. at each temperature, Figure 2) have shown that the four catalysts reduced at $350\text{ }^{\circ}\text{C}$ present very different $\text{Co}_{hcp}/\text{Co}_{fcc}$ ratios. Even if the Co_2C transformation to Co_{hcp} is generally performed sequentially, it has been reported that the Co_{hcp} metallic phase is produced under H_2+CO atmosphere in the case of Co/CNF catalysts [68]. It is thus reasonable to propose that the concomitant presence of CO and H_2 in the gas phase during the reduction step should contribute to an increase of the $\text{Co}_{hcp}/\text{Co}_{fcc}$ ratio. Thus, the high $\text{Co}_{hcp}/\text{Co}_{fcc}$ ratio measured for the *ex-nitrate* catalysts could be associated to the higher amount of CO-releasing groups in these materials. Figure 5b shows the excellent correlation between the amount of CO-releasing groups and the $\text{Co}_{hcp}/\text{Co}_{fcc}$ ratio. This offers real perspectives to control the $\text{Co}_{hcp}/\text{Co}_{fcc}$ ratio in Co/C catalysts by controlling the gaseous atmosphere during the *in situ* reduction of the catalysts.

Quinone groups and their influence on hydrogen spillover.

H-spillover is a potential handle to enhance hydrogen storage in CNT, and such enhancement has been often reported for cobalt-based supported materials [69–71]. In order to assess the H-spillover, H_2 -TPD-MS analyses of the catalysts (Figure 4c) are very informative. No peak related to H_2 desorption was observed for the CNT support. The H_2 desorption profiles of all the catalysts show two main large peaks. The first peak between 400 and $800\text{ }^{\circ}\text{C}$ is due to H_2 release from the Co particles [9]. However, if we consider the H_2 quantities released (Table 3) for the calculation of the metal particle size ($\text{Co}_{N-W}/\text{CNT} = 2.0\text{ nm}$; $\text{Co}_{N-E}/\text{CNT} = 1.3\text{ nm}$; $\text{Co}_{A-W}/\text{CNT} = 2.2\text{ nm}$; and $\text{Co}_{A-EW}/\text{CNT} = 2.3\text{ nm}$), it is evident that H_2 amounts are too high to correspond only to the Co adsorbed H_2 . Particularly, the $\text{Co}_{N-E}/\text{CNT}$ catalyst, which presents the larger mean particle size and the lower reduction degree releases the highest amount of H_2 . Consequently, this peak should also integrate the hydrogen desorbed *via* reverse H-spillover [72], which is the migration of H atoms from the support onto the cobalt particles, where they recombine into H_2 that desorbs [9]. Considering the fact that the mean cobalt particle sizes as

determined by TEM and XRD are in good agreement (Table 1), we used the TEM values and the cobalt reduction degree (from *in-situ* XRD) to estimate what should be the theoretical amount of H₂ that should desorb from these particles in the absence of reverse H-spillover (Table 3). Then, we used these latter values to estimate the H₂ evolution linked to reverse H-spillover. It is also interesting to note that H₂ desorption was observed at 350 °C during the TPD-MS analyses performed during the catalyst reduction step (Figure S14). This desorption peak was particularly intense for the Co_{N-E}/CNT catalyst. In that case, H₂ desorption should be mainly associated to reverse H-spillover, since the peak was of very low intensity or even absent for the other catalysts.

The second peak of the H₂-TPD-MS analyses of the catalysts (absent in the case of the original support) that starts at ~ 800 °C is associated to the decomposition (without the help of the supported metal) of stable C-H functionalities, which have been created by H-spillover from the metallic particles [73]. From the values reported on Table 3, the H-spillover is more pronounced on the Co_{N-E}/CNT catalyst. This result can be rationalized by considering the fact that on carbon-supported catalysts, the hydrogen spillover is enhanced on supports presenting a high amount of surface oxygen groups [10], and particularly quinone groups [74]. Since quinone groups cannot be distinguished from other carbonyl groups by TPD, we rely on XPS analyses performed on the calcined catalysts to determine their concentration. The deconvoluted O 1s XPS spectra of the catalysts, presented on Figure S15, and Table S6, show the results of these deconvolutions (the quantification of each type of surface species was made base on the FWHM of the peaks) [15]. The O 1s region of the four catalysts is composed of three components, corresponding to quinone surface groups (~ 529.8 eV), C=O containing surface groups (~ 531.3 eV) and C–O surface groups (~ 532.9 eV) [75,76].

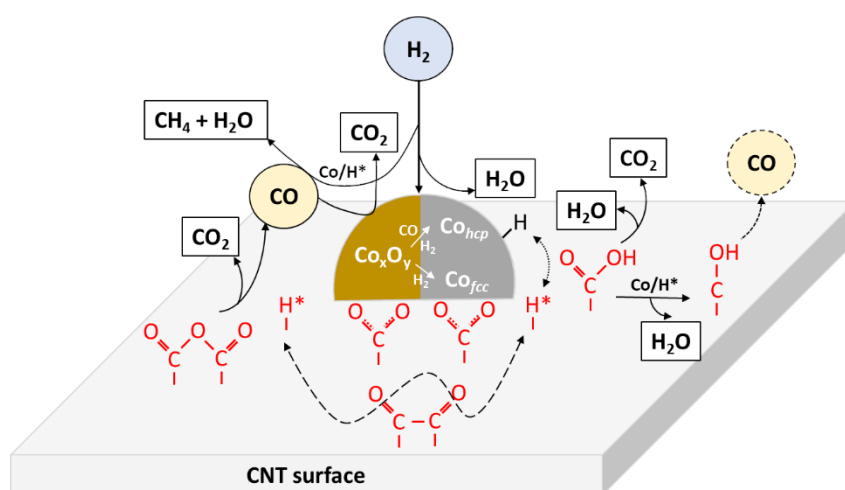
Table 3. Results of the deconvolution of H₂ TPD spectra of Co/CNT catalysts.

Catalyst	H ₂ peak (400-800 °C) ^{a)}	H ₂ from Co ^{b)}	H ₂ from reverse H-spillover ^{c)} ($\mu\text{mol.g}^{-1}$)	Total spillover ^{d)}	H ₂ total ^{e)}
Co _{N-W} /CNT	700	343	357	1149	1493
Co _{N-E} /CNT	970	475	495	1575	2050
Co _{A-W} /CNT	590	322	268	1455	1777
Co _{A-EW} /CNT	620	546	74	1019	1565

a) H₂ quantities released between 400 and 800 °C. b). Theoretical amount of H₂ that should desorb from Co particles (in the absence of reverse H-spillover) estimated from TEM particle size and cobalt reduction degree (from *in-situ* XRD). c) Amount of H₂ obtained by abstracting the values of column 2 from the values of column 2. d) Sum of H₂ quantities released between 800 and 1070 °C and H₂ from reverse H-spillover. e) Total H₂ quantities released between 400 and 1070 °C (sum of values of column 3 and column 5).

Figure 5c shows the correlation between the amount of quinone groups on the support and the total amount of H₂ desorbed from spillover. Obviously, a higher concentration in quinone groups favors the H-spillover. Even if the Co_{N-E}/CNT catalyst presents a higher H-spillover, it is worth mentioning that these species are not reactive enough to contribute to a high degree of reduction of this catalyst, this latter being dictated mainly by the strength of the MSI.

The most relevant findings on our analysis on the role of carbon surface chemistry and H-spillover on the final features of the reduced Co/CNT catalysts are resumed on Scheme 1.



Scheme 1. Most relevant phenomena occurring during Co/CNT catalyst reduction.

CNT surface oxidation by nitric acid creates various functional groups. The carboxylic groups contribute to cobalt particle stabilization, and a strong cobalt-carboxylate interface contributes to a decrease of the reduction degree of cobalt. These groups can decompose to CO₂ or be reduced to phenol groups (either by the cobalt or by the spilled over H* species). The carboxylic anhydrides decompose at relatively low temperature to produce CO and CO₂. The evolved CO, which could also arise from phenol group decomposition, is consumed together with H₂ either to produce Co_{hcp}, or to produce methane by methanation (either by the cobalt or by the spilled

over H* species). The quinone groups constitute efficient shuttles for hydrogen spillover on the CNT surface. All these phenomena are particularly present in the case of the *ex*-nitrate catalysts, for which surface oxidation occurs during the calcination step due to nitrogen oxide evolution. After having demonstrated the impact of the chemistry operating during catalyst elaboration on the catalysts features it is important to rationalize these effects in the context of the FTS.

3.2 Structure/performance correlations

Catalytic Performances in FTS. Figure 6a shows the CTY evolution ($\text{mol}_{\text{CO}} \cdot \text{mol}_{\text{Co}}^{-1} \cdot \text{s}^{-1}$) as a function of time-on-stream (TOS, h) for the four catalysts during FTS at 20 bar, 220 °C, $\text{H}_2/\text{CO} = 2 \text{ v/v}$, GHSV = 1100-2300 $\text{mL} \cdot \text{g}^{-1} \cdot \text{h}^{-1}$. The average deactivation parameter ($r_i/r_{54\text{h}}$, ratio of the initial rate to the rate at steady state (after 54 h TOS), as well as the average sintering parameter of Co particles (d calculated based on mean particle size obtained by TEM of the fresh and spent catalysts) are also presented on this figure. The lower catalytic performances obtained in this work as compared to those reported by de Jong *et al.* [14,77] for 9%Co/CNT catalysts in microreactors under similar conditions can be explained by the use of a microchannel FT reactor [78]. The results from the catalytic tests revealed significant differences in the performances (activity, selectivity and stability) of the studied catalysts (Figure 6 and Table 4). For the *ex*-nitrate cobalt catalysts, higher activities were found for the systems impregnated with ethanol, as reported in the work of de Jong *et al.* [14] In the case of the *ex*-acetate catalysts, the catalyst prepared in water performed significantly better than the one prepared in the ethanol/water mixture. Overall, the activity order follows: $\text{Co}_{N-E}/\text{CNT} > \text{Co}_{A-W}/\text{CNT} \approx \text{Co}_{N-W}/\text{CNT} > \text{Co}_{A-EW}/\text{CNT}$.

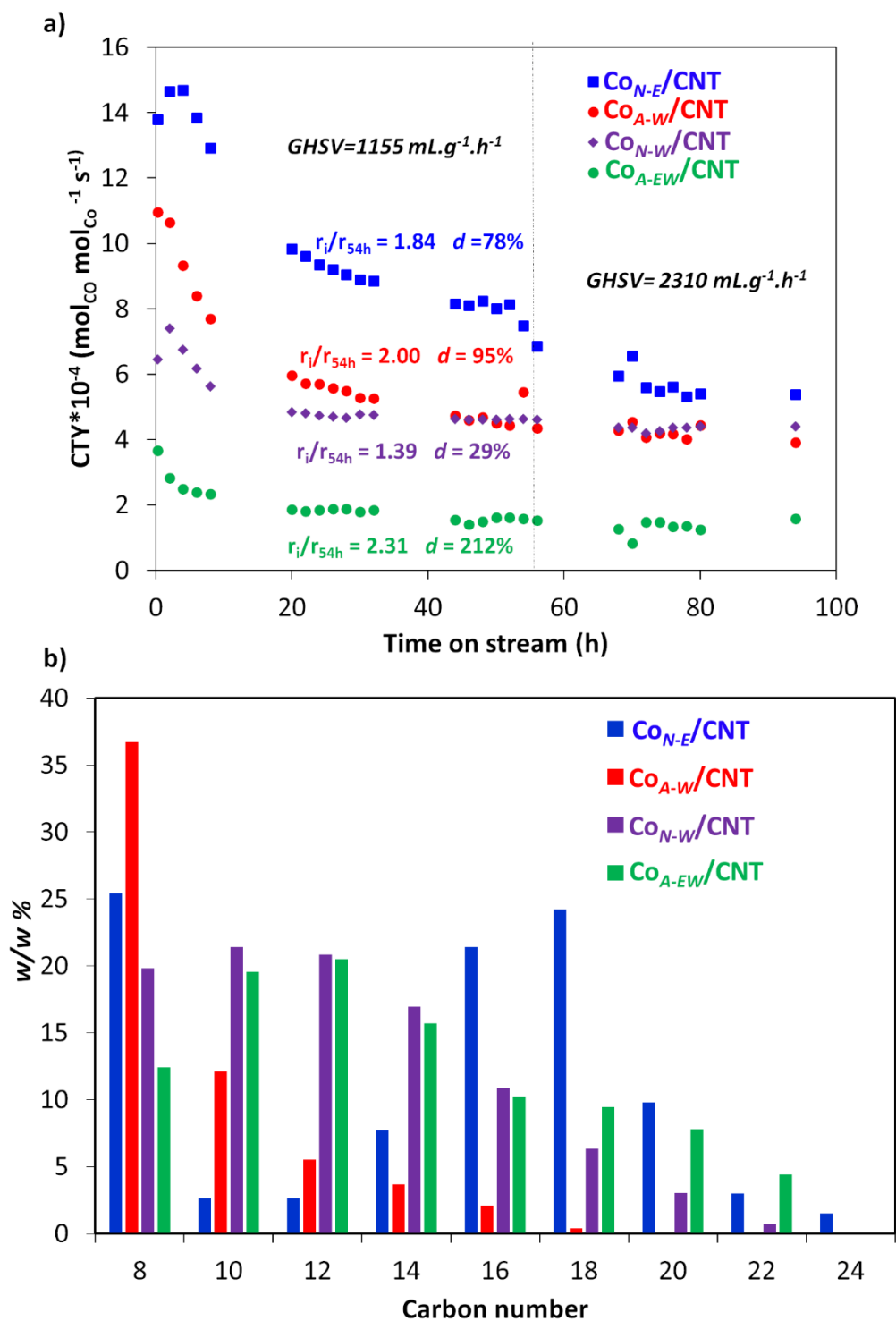


Figure 6. FTS catalytic performances of the Co/CNT catalysts: a) CTY as a function of TOS; and b) liquid product distribution.

Table 4. FTS catalytic performances of the Co/CNT catalysts.

Catalyst	CO ^{a)} (%)	CTY _i ^{b)}	CTY _f ^{c)}	TOF ^{d)}	TOF _{corr.} ^{e)} (10 ⁻³ .s ⁻¹)	TOF ^{f)}	TEM ^{g)} (nm)	S _{CH4} (%)	S _{C2-C4} (%)	S _{C5+} (%)	O/P	α	r _i /r _{54h}	d (%)
Co _{N-W} /CNT	48	6.4	4.5	3.8	6.0	3.4	8	13	6.5	81	0.11	0.85	1.4	29
Co _{N-E} /CNT	87	13.8	6.9	7.2	14.8	6.5	10	14	5.3	80	0.05	0.88	1.8	78
Co _{A-W} /CNT	64	10.9	4.5	4.7	5.4	3.8	9	13	4.8	82	0.07	0.61	2	95
Co _{A-EW} /CNT	23	3.6	1.46	1.1	1.3	1.3	10	13	7.3	80	0.38	0.74	2.3	212

^{a)} Initial CO conversion. ^{b)} Initial CTY (in 10⁻⁴ mol_{CO}.mol_{Co}⁻¹.s⁻¹). ^{c)} Final CTY (in 10⁻⁴ mol_{CO}.mol_{Co}⁻¹.s⁻¹). ^{d)} Initial TOF. ^{e)} Initial TOF after correction on the basis of the reduction degree. ^{f)} Final TOF. ^{g)} TEM particle size of spent catalysts. .

Regarding the selectivity to higher hydrocarbons, similar C_{5+} selectivity's were found for all the catalysts (80-82%), which could be related to similar particle size measured after catalysis for all catalysts (8-10 nm, Table 4). However, the chain growth probability factor (α) was higher for *ex*-nitrate catalysts (0.85-0.88) than for *ex*-acetate ones (0.61-0.74).

As far as stability is concerned, the average deactivation parameter follows the order: $Co_{A-E}/CNT > Co_{A-W}/CNT > Co_{N-E}/CNT > Co_{N-W}/CNT$; and the average sintering parameter follows the same order.

These results show that the catalyst prepared from the nitrate precursor in ethanol is the most efficient, while that prepared from acetate precursor in ethanol/water mixture is the less efficient. The two other catalysts, Co_{A-W}/CNT and Co_{N-W}/CNT show similar performances in terms of activity, selectivity to C_{5+} and stability at steady state, but the Co_{N-W}/CNT catalyst allows reaching a higher α value.

Structure/performance relationships.

Classical descriptors of Co-based FTS catalyst performances include cobalt particle size [79], crystallographic phase [80], interaction with the support and reducibility [81,82], and confinement [22,83]. We have shown that these features of the Co/CNT catalysts are intimately linked to the surface chemistry of the support. In the case of Co/CNT catalysts, the confinement effects are often presented as a determining factor for catalyst activity. Thus, a high TOF should be obtained with a Co/CNT catalyst presenting a high filling yield, a high proportion of Co_{hcp} , a high degree of reduction, a high spillover, and a Co particle size $> 6-8$ nm [79,84]. It is clear from the data reported in Table 1 and Figure 7a, which resumes the main catalyst features on a 0-1 scale, that none of the prepared catalysts presents maximum values over all the criteria considered. Two catalysts with very different profiles can be distinguished. The first one is the Co_{N-E}/CNT catalyst, which even if it presents the lowest reduction degree, is very well

positioned for as far as all the other criteria are concerned, and presents the highest TOF. The second one is the Co_{A-EW}/CNT catalyst, which exhibits a high degree of reduction, but is poorly positioned for all other criteria, and leads to the lowest TOF value.

As most of the catalyst features reported on Figure 7a are related to the fresh catalysts, we rely on the values of the initial TOF (calculated with initial Co particle size) corrected from the cobalt reduction degree (TOF_{corr.}, Table 4) to draw structure/activity correlations. We tried to correlate the different features of the catalysts shown on Figure 7a, both independently or in combination with the TOF values. As expected [8], poor (or no) correlations exist between the TOF and each of the parameters considered independently (Figure S16). Only the cobalt filling yield can be roughly related to the TOF_{corr.} (coefficient of determination R² = 0.8012). We tried also correlations with only two or three parameters. When using two parameters (Figure S17), the best correlation (R² = 0.9877) included also the cobalt filling yield and surprisingly the inverse of the cobalt initial particle size. A correlation was also found including the cobalt filling yield and the H-spillover (R² = 0.9554). When using three parameters (Figure S18), the best correlation (R² = 0.9906) included the three previously considered catalyst features: the cobalt filling yield, inverse of the cobalt initial particle size and H-spillover. The best correlation (R² = 0.9943, Figure 7b) is the one obtained by combining four parameters: the percentage of Co_{hcp}, the filling yield, the H-spillover amount, and the inverse of the cobalt initial particle size. It is not surprising to integrate in such correlation the Co_{hcp}, the confinement degree and the extent of H-spillover, since it has been shown that all these features positively affect the catalytic activity. The fact that the TOF should increase at lower particle size is surprising, and in fact goes against what has been shown in the literature for Co particles for which the TOF is increased with particle size up to about 6-10 nm, after which it remains stable [79,84]. It is nevertheless necessary to integrate a decisive element, namely that this general tendency reported for cobalt in the literature does not concern confined metallic particles. Thus, the trend

observed in our work may be linked to the fact that the most active particles being those that are confined, the evolution of the TOF with their size (in the 3-7 nm range) does not follow the previously established rule. The reason of the lower TOF generally reported on small unconfined Co particles (< 6-8 nm) is the strong adsorption of CO on edge/corner sites, as well as a lower intrinsic activity at the terraces [84]. This could not be the case for confined Co_{hcp} particles. Indeed, although CO adsorption is stronger on Co_{hcp} particles than on Co_{fcc} ones [85], the Co_{hcp} particles are more active. Additionally, different trends in TOF according to cobalt particle size were reported in the case of Co_{fcc} and Co_{hcp} particles [86], and to the best of our knowledge, no clear correlation between TOF and particle size has been reported up to now in the literature for Co_{hcp} in FTS. As far as confined particles are concerned, it is noteworthy that confinement can lead to downshifted d -band states, and consequently to weaker adsorption energy of adsorbates as CO [87]. It seems reasonable that a modification of the energy landscape in a confined environment and the fact that a large fraction of our catalysts contain Co_{hcp} are at the origin of the correlation found. It is the combined effects of a smaller initial cobalt particle size and a higher hydrogen spillover that can explain the higher initial TOF (corrected from the cobalt reduction degree) measured for the $\text{Co}_{A-W}/\text{CNT}$ catalyst as compared to the $\text{Co}_{N-W}/\text{CNT}$ one.

In FTS, the catalyst stability is impacted by several factors such as metal sintering (coalescence and Ostwald ripening), cobalt oxidation, and carbon deposition, which negatively affect the rate [88,89], or carbide formation, CO reduction, and restructuring of the surface, which have a positive influence [90]. In the case of Co/CNT catalysts, cobalt re-oxidation, cobalt-support interactions, wax accumulation and sintering have been identified as the main sources of catalyst deactivation [31,91,92]. In our study, the catalyst stability is expressed as the average deactivation parameter (r_i/r_{54h}).

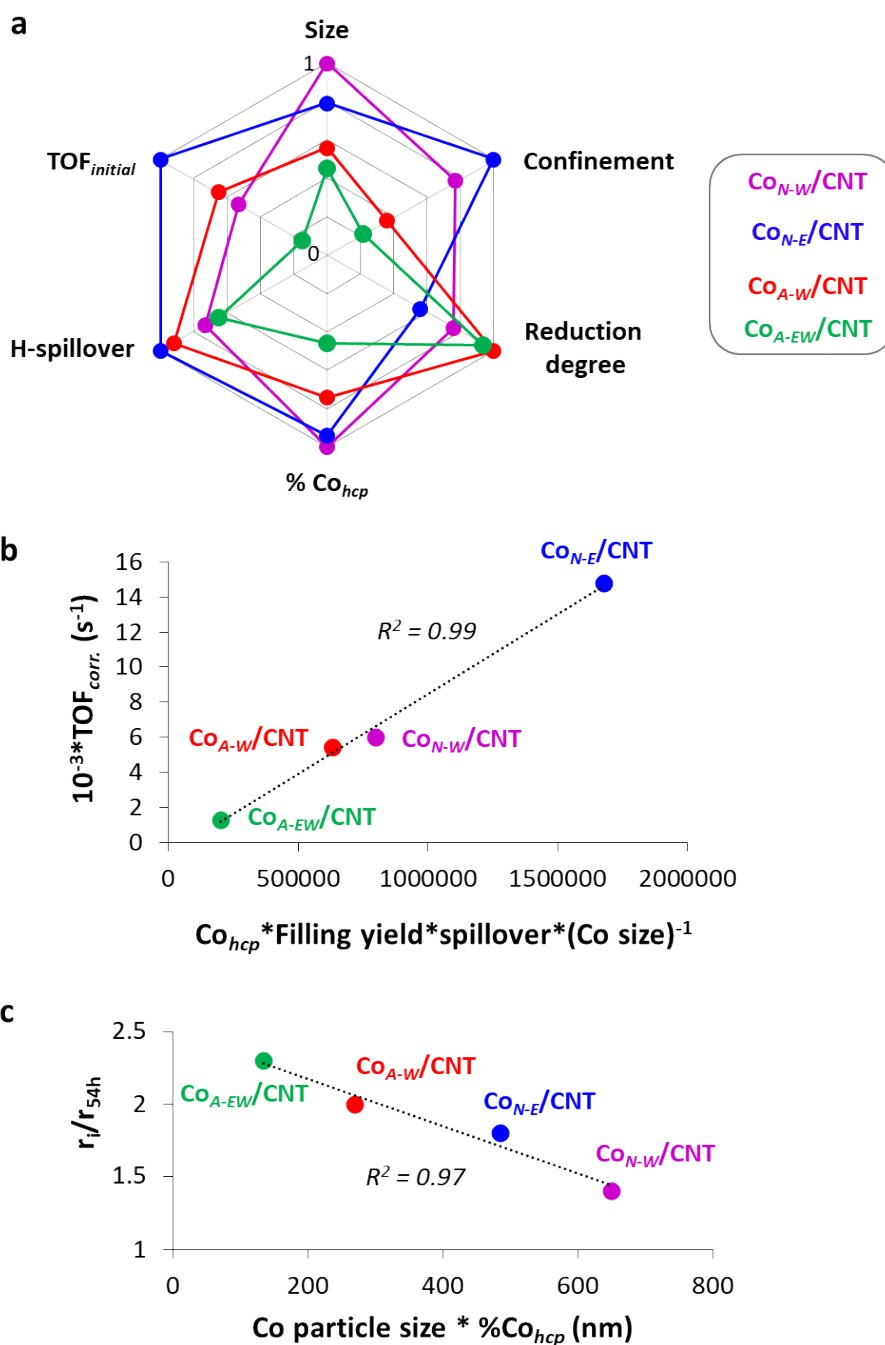


Figure 7. a) Main catalyst features and performances on a 0-1 scale; b) structure/activity correlation; and c) structure/stability correlation.

We tried to correlate the different features of the catalysts shown on Figure 7a, both independently or in combination with the deactivation parameter. The best correlation (Figure 7c) was obtained by combining the initial particle size and the percentage of Co_{hcp} in the catalysts. This good correlation could be tentatively rationalized by the fact that sintering [93]

and cobalt oxidation [94] should be favored with small cobalt particles [95]. Furthermore, the high stability of the Co_{hcp} phase under FTS conditions has been reported [66,67,96,97], and some studies have pointed out that this phase is more stable under FTS conditions than the Co_{fcc} one [98,99]. Finally, for the *ex*-nitrate catalysts containing a significant amount of confined particles, we noticed a template effect of the CNT cavity, since the sintering was more pronounced for the Co particles located on the external surface of the CNT (Figure S19).

CONCLUSIONS

Oxidized CNT were used to support cobalt particles (3-7 nm). Co/CNT catalysts were prepared in two different solvents (water and ethanol) from two different precursors (nitrate and acetate). The use of ethanol, which presents a lower surface tension than water, allowed reaching higher metal dispersion. The lower filling yield obtained for the *ex*-acetate catalysts could be related to the ability of acetate ions to interact with the oxidized CNT external surface *via* deprotonation of surface –OH groups. A rigorous characterization of the catalysts at different stages of their preparation shows that the surface chemistry, which operates between the cobalt precursor and the surface of the support, affects many characteristics of the final catalyst, such as: the metal-support interaction, the $\text{Co}_{hcp}/\text{Co}_{fcc}$ ratio and the extent of hydrogen spillover. Particularly, the oxygenated groups of the support, either present on the initial support or created during the preparation of the catalyst, strongly contribute to the catalyst features. The CO_2 releasing groups contribute to stabilize Co particles and reduce their reducibility, while the CO releasing groups contribute to increase the $\text{Co}_{hcp}/\text{Co}_{fcc}$ ratio and hydrogen spillover (quinone groups). The prepared catalysts present very different features (Co reduction degree, confinement, crystal phase, particle size, H-spillover), and accordingly different activity and stability in FTS. The selectivity to higher hydrocarbons ($\text{S}_{\text{C}_{5+}}$) is similar for all the catalysts, which can be rationalized by a similar Co particle size for the spent catalysts. The differences in initial activity

and stability have been rationalized considering catalyst structures. Interestingly, our correlation results show that the initial TOF increases for smaller particle size, which is in contrast to what is generally found for Co_{fcc}/C catalysts. This has been tentatively interpreted by an increased contribution of the confinement effect of Co_{hcp} particles. Finally, the stability of the catalyst is mainly affected by the initial Co particle size and the percentage of Co_{hcp} . These results show that the design of high-performance FT catalysts remains challenging, and that an optimal combination of all catalyst features (not obtained in this study) requires a fine control of number of parameters related to the preparation of the catalytic system. Last but not least, in the structure-performance correlations presented in this study, the contribution of the different factors has not been modulated. This has not prevented excellent correlations to be obtained. Attributing different weight coefficients could also be sound, and also lead to different correlations. However, this would need the use of dedicated algorithms, which is outside the scope of the present article that aims, for the first time, at demonstrating that complex relations should be considered in order to rationalize the behavior of the Co based catalysts in FTS.

ASSOCIATED CONTENT

Supporting Information. Additional catalyst characterization (TEM, HRTEM, TPD, XPS, TPR, TGA, VSM, adsorption and desorption isotherms of ethanol and water).

AUTHOR INFORMATION

Author Contributions

The manuscript was written through contributions of all authors. All authors have given approval to the final version of the manuscript.

Funding Sources

This research (CatFisch project) was funded by the “Région Occitanie” and the University of Toulouse (France). B.F.M. acknowledges the exploratory project under the Fundação para a Ciência e a Tecnologia (FCT, Portugal) Investigator Programme (ref. IF/00301/2015) with financial support from FCT/MCTES, through national funds (PIDDAC).

ACKNOWLEDGMENTS

The authors thank V. Collière (LCC), S. Patry (RAPSODEE), D. Marty (RAPSODEE), M. Ribeiro (RAPSODEE) and P. Bertorelle (RAPSODEE) for technical support.

Competing interests

The authors declare no competing interests.

REFERENCES

- [1] J. Sun, G. Yang, X. Peng, J. Kang, J. Wu, G. Liu, N. Tsubaki, Beyond Cars: Fischer-Tropsch Synthesis for Non-Automotive Applications, *ChemCatChem*. 11 (2019) 1412–1424. doi:10.1002/cctc.201802051.
- [2] M.E. Dry, The Fischer-Tropsch process: 1950-2000, *Catal. Today*. 71 (2002) 227–241. doi:10.1016/S0920-5861(01)00453-9.
- [3] Z. Qi, L. Chen, S. Zhang, J. Su, G.A. Somorjai, A mini review of cobalt-based nanocatalyst in Fischer-Tropsch synthesis, *Appl. Catal. A Gen.* 602 (2020) 117701. doi:10.1016/j.apcata.2020.117701.
- [4] Z. Gholami, Z. Tišler, V. Rubáš, Recent advances in Fischer-Tropsch synthesis using cobalt-based catalysts: a review on supports, promoters, and reactors, *Catal. Rev. - Sci. Eng.* (2020) 1–84. doi:10.1080/01614940.2020.1762367.
- [5] Z. Gholami, N. Asmawati Mohd ZabiDi, F. Gholami, O.B. Ayodele, M. Vakili, The influence of catalyst factors for sustainable production of hydrocarbons via Fischer-Tropsch synthesis, *Rev. Chem. Eng.* 33 (2017) 337–358. doi:10.1515/revce-2016-0009.
- [6] J. Van De Loosdrecht, M. Datt, J.L. Visagie, Carbon coated supports for cobalt based fischer-tropsch catalysts, *Top. Catal.* 57 (2014) 430–436. doi:10.1007/s11244-013-0198-8.
- [7] C. Liu, Y. He, L. Wei, Y. Zhang, Y. Zhao, J. Hong, S. Chen, L. Wang, J. Li, Hydrothermal carbon-coated TiO₂ as support for Co-based catalyst in Fischer-Tropsch synthesis, *ACS Catal.* 8 (2018) 1591–1600. doi:10.1021/acscatal.7b03887.
- [8] A.C. Ghogia, A. Nzihou, P. Serp, K. Soulantica, D.P. Minh, Cobalt catalysts on carbon-based materials for Fischer-Tropsch synthesis: a review, *Appl. Catal. A Gen.* (2020) 117906. doi:10.1016/j.apcata.2020.117906.
- [9] A.C. Ghogia, S. Cayez, B.F. Machado, A. Nzihou, P. Serp, K. Soulantica, D. Pham Minh, Hydrogen Spillover in the Fischer-Tropsch Synthesis on Carbon-supported Cobalt Catalysts, *ChemCatChem*. 12 (2020) 1–13. doi:10.1002/cctc.201901934.
- [10] I.C. Gerber, P. Serp, A theory/experience description of support effects in carbon-supported catalysts, *Chem. Rev.* 120 (2020) 1250–1349. <http://pubs.acs.org/doi/10.1021/acs.chemrev.9b00209> (accessed October 9, 2019).
- [11] A. Sims, M. Jeffers, S. Talapatra, K. Mondal, S. Pokhrel, L. Liang, X. Zhang, A.L. Elias, B.G. Sumpter, V. Meunier, M. Terrones, Hydro-deoxygenation of CO on functionalized carbon nanotubes for liquid fuels production, *Carbon N. Y.* 121 (2017) 274–284. doi:10.1016/j.carbon.2017.05.094.
- [12] H. Xiong, M.A.M.M. Motchelaho, M. Moyo, L.L. Jewell, N.J. Coville, Correlating the preparation and performance of cobalt catalysts supported on carbon nanotubes and carbon spheres in the Fischer-Tropsch synthesis, *J. Catal.* 278 (2011) 26–40. doi:10.1016/j.jcat.2010.11.010.
- [13] T.O. Honsho, T. Kitano, T. Miyake, T. Suzuki, Fischer-Tropsch synthesis over Co-loaded oxidized diamond catalyst, *Fuel*. 94 (2012) 170–177. doi:10.1016/j.fuel.2011.08.045.

- [14] T.O. Eschemann, W.S. Lamme, R.L. Manchester, T.E. Parmentier, A. Cognigni, M. Rønning, K.P. De Jong, Effect of support surface treatment on the synthesis, structure, and performance of Co/CNT Fischer-Tropsch catalysts, *J. Catal.* 328 (2015) 130–138. doi:10.1016/j.jcat.2014.12.010.
- [15] R.C. Contreras, B. Guicheret, B.F. Machado, C. Rivera-Cárcamo, M.A. Curiel Alvarez, B. Valdez Salas, M. Rutttert, T. Placke, A. Favre Réguillon, L. Vanoye, C. de Bellefon, R. Philippe, P. Serp, Effect of mesoporous carbon support nature and pretreatments on palladium loading, dispersion and apparent catalytic activity in hydrogenation of myrcene, *J. Catal.* 372 (2019) 226–244. doi:10.1016/j.jcat.2019.02.034.
- [16] T.T. Nguyen, P. Serp, Confinement of metal nanoparticles in carbon nanotubes, *ChemCatChem*. 5 (2013) 3595–3603. doi:10.1002/cctc.201300527.
- [17] D. Schanke, S. Vada, E.A. Blekkan, A.M. Hilmen, A. Hoff, A. Holmen, Study of Pt-promoted cobalt CO hydrogenation catalysts, *J. Catal.* 156 (1995) 85–95. doi:10.1006/jcat.1995.1234.
- [18] M. Repoux, Comparison of background removal methods for XPS, *Surf. Interface Anal.* 18 (1992) 567–570.
- [19] M. Verelst, T.O. Ely, C. Amiens, E. Snoeck, P. Lecante, A. Mosset, M. Respaud, J.M. Broto, B. Chaudret, Synthesis and characterization of CoO, Co₃O₄, and mixed Co/CoO nanoparticles, *Chem. Mater.* 11 (1999) 2702–2708. doi:10.1021/cm991003h.
- [20] A. Aznárez, A. Gil, S.A. Korili, Performance of palladium and platinum supported on alumina pillared clays in the catalytic combustion of propene, *RSC Adv.* 5 (2015) 82296–82309. doi:10.1039/c5ra15675k.
- [21] J. Scalbert, I. Cléménçon, C. Legens, F. Diehl, D. Decottignies, S. Maury, Development of an innovative XRD-DRIFTS prototype allowing operando characterizations during Fischer-Tropsch synthesis over cobalt-based catalysts under representative conditions, *Oil Gas Sci. Technol. – Rev. d’IFP Energies Nouv.* 70 (2015) 419–428. doi:10.2516/ogst/2014031.
- [22] O. Akbarzadeh, N.A.M. Zabidi, Y.A. Wahab, N.A. Hamizi, Z.Z. Chowdhury, Z.M.A. Merican, M.A. Rahman, S. Akhter, E. Rasouli, M.R. Johan, Effect of cobalt catalyst confinement in carbon nanotubes support on Fischer-Tropsch synthesis performance, *Symmetry (Basel)*. 10 (2018) 572. doi:10.3390/sym10110572.
- [23] K. Narasimharao, B.M. Abu-Zied, S.Y. Alfaifi, Cobalt oxide supported multi wall carbon nanotube catalysts for hydrogen production via sodium borohydride hydrolysis, *Int. J. Hydrogen Energy*. (2020). doi:10.1016/j.ijhydene.2020.11.112.
- [24] X. Liu, X. Lu, R. Wang, H. Zhou, S. Xu, Surface complexes of acetate on edge surfaces of 2:1 type phyllosilicate: Insights from density functional theory calculation, *Geochim. Cosmochim. Acta.* 72 (2008) 5896–5907. doi:10.1016/j.gca.2008.09.026.
- [25] M.A. Ahmad, B. Prelot, J. Zajac, Calorimetric screening of co-operative effects in adsorption of Co(II) on γ -alumina surface in the presence of Co-complexing anions in aqueous solution, *Thermochim. Acta.* 694 (2020) 178800. doi:10.1016/j.tca.2020.178800.
- [26] J.-P. Tessonnier, O. Ersen, G. Weinberg, C. Pham-Huu, D.S. Su, R. Schlögl, Selective deposition of metal nanoparticles inside or outside multiwalled carbon nanotubes., *ACS*

- Nano. 3 (2009) 2081–2089. doi:10.1021/nn900647q.
- [27] H. Park, Y. Kim, H. Youn, H. Choi, Y. Kim, Auto-Reduction Behavior of cobalt on graphitic carbon nitride coated alumina supports for Fischer – Tropsch synthesis, *ChemCatChem*. 9 (2017) 4098–4104. doi:10.1002/cctc.201700613.
- [28] M. Trépanier, A.K. Dalai, N. Abatzoglou, Synthesis of CNT-supported cobalt nanoparticle catalysts using a microemulsion technique: Role of nanoparticle size on reducibility, activity and selectivity in Fischer-Tropsch reactions, *Appl. Catal. A Gen.* 374 (2010) 79–86. doi:10.1016/j.apcata.2009.11.029.
- [29] M. Wolf, B.K. Mutuma, N.J. Coville, N. Fischer, M. Claeys, Role of CO in the water-induced formation of cobalt oxide in a high conversion Fischer–Tropsch environment, *ACS Catal.* 8 (2018) 3985–3989. doi.org/10.1021/acscatal.7b04177.
- [30] T. Jaumann, E. M. M. Ibrahim, S. Hampel, D. Maier, A. Leonhardt, B. Büchner, The synthesis of superparamagnetic cobalt nanoparticles encapsulated in carbon through high-pressure CVD, *Chem. Vap. Deposition* 19 (2013) 228-234. doi.org/10.1002/cvde.201207020.
- [31] S. Chernyak, A. Burtsev, S. Maksimov, S. Kupreenko, K. Maslakov, S. Saviylov, Structural evolution, stability, deactivation and regeneration of Fischer-Tropsch cobalt-based catalysts supported on carbon nanotubes, *Appl. Catal. A Gen.* 603 (2020) 117741. doi:10.1016/j.apcata.2020.117741.
- [32] T.N. Phaahlamohlaka, D.O. Kumi, M.W. Dlamini, R. Forbes, L.L. Jewell, D.G. Billing, N.J. Coville, Effects of Co and Ru intimacy in Fischer-Tropsch catalysts using hollow carbon sphere supports: assessment of the hydrogen spillover processes, *ACS Catal.* 7 (2017) 1568–1578. doi:10.1021/acscatal.6b03102.
- [33] O. Akbarzadeh, N.A.M. Zabidi, Z.M.A. Merican, S. Sagadevan, A. Kordijazi, S. Das, A.A. Babadi, M.A. Rahman, N.A. Hamizi, Y.A. Wahab, M.R. Johan, Effect of manganese on Co-Mn/CNT bimetallic catalyst performance in Fischer-Tropsch reaction, *Symmetry (Basel)*. 11 (2019) 1–19. doi:10.3390/sym11111328.
- [34] W. Chen, Z. Fan, X. Pan, X. Bao, Effect of confinement in carbon nanotubes on the activity of Fischer–Tropsch iron catalyst, *J. Am. Chem. Soc.* 130 (2008) 9414–9419. doi:10.1021/ja8008192.
- [35] Y. Zhu, Y. Ye, S. Zhang, M.E. Leong, F. Tao, Synthesis and catalysis of location-specific cobalt nanoparticles supported by multiwall carbon nanotubes for Fischer-Tropsch synthesis, *Langmuir*. 28 (2012) 8275–8280. doi:10.1021/la300607k.
- [36] C. Rivera-Cárcamo, C. Scarfiello, A.B. García, Y. Tison, H. Martinez, W. Baaziz, O. Ersen, C. Le Berre, P. Serp, Stabilization of metal single atoms on carbon and TiO₂ supports for CO₂ hydrogenation: the importance of regulating charge transfer, *Adv. Mater. Interfaces*. (2020) 2001777. doi:10.1002/admi.202001777.
- [37] J.L. Figueiredo, M.F.R. Pereira, M.M.A. Freitas, J.J.M. Órfão, Characterization of active sites on carbon catalysts, *Ind. Eng. Chem. Res.* 46 (2007) 4110–4115. doi:10.1021/ie061071v.
- [38] J. Castillo, L.E. Arteaga-Pérez, A. Karelavic, R. Jiménez, The consequences of surface heterogeneity of cobalt nanoparticles on the kinetics of CO methanation, *Catal. Sci. Technol.* 9 (2019) 6415–6427. doi:10.1039/c9cy01753d.

- [39] T. Wang, Y. Ding, J. Xiong, L. Yan, H. Zhu, Y. Lu, L. Lin, Effect of vanadium promotion on activated carbon-supported cobalt catalysts in Fischer – Tropsch synthesis, *Catal. Letters*. 107 (2006) 47–52. doi:10.1007/s10562-005-9730-1.
- [40] P. Serp, CHAPTER 1 -Carbon (Nano) materials for Catalyst, in: *Nanostructured Carbon Mater. Catal.*, Royal Society of Chemistry, 2015: pp. 1–45. doi:10.1039/9781782622567.
- [41] F. Z-scheme, N. Yb, A.S. O, Y. Er, Functionalization of porous carbons for catalytic applications, *J. Mater. Chem. A*. (2013) 2–32. doi:10.1039/c7ta07529d.
- [42] G. Peng, F. Gramm, C. Ludwig, F. Vogel, Effect of carbon surface functional groups on the synthesis of Ru/C catalysts for supercritical water gasification, *Catal. Sci. Technol.* 5 (2015) 3658–3666. doi:10.1039/c5cy00352k.
- [43] M. Kang, M.W. Song, K.L. Kim, Palladium Catalysts supported on activated carbone with different textural and surface chemical properties, *React. Kinet. Catal. Lett.* 53 (2019) 1689–1699.
- [44] M.C. Román-Martínez, D. Cazorla-Amorós, A. Linares-Solano, C.S.M. nez De Lecea, H. Yamashita, M. Anpo, Metal-support interaction in Pt/C catalysts. Influence of the support surface chemistry and the metal precursor, *Carbon N. Y.* 33 (1995) 3–13. doi:10.1016/0008-6223(94)00096-I.
- [45] B. Zhang, D.S. Su, Probing the metal-support interaction in carbon-supported catalysts by using electron microscopy, *ChemCatChem*. 7 (2015) 3639–3645. doi:10.1002/cctc.201500666.
- [46] P. Serp, E. Castillejos, Catalysis in carbon nanotubes, *ChemCatChem*. 2 (2010) 41–47. doi:10.1002/cctc.200900283.
- [47] P. Dibandjo, C. Zlotea, R. Gadiou, C. Matei Ghimbeu, F. Cuevas, M. Latroche, E. Leroy, C. Vix-Guterl, Hydrogen storage in hybrid nanostructured carbon/palladium materials: Influence of particle size and surface chemistry, *Int. J. Hydrogen Energy*. 38 (2013) 952–965. doi:10.1016/j.ijhydene.2012.10.050.
- [48] P. Serp, Carbon. In *Comprehensive Inorganic Chemistry II (Second Edition)*, in: J. Reedijk, K. Poeppelmeier (Eds.), Elsevier, Oxford, 2013: pp. 323–369. doi:10.1016/B978-0-08-097774-4.00221-7.
- [49] T. Wanjun, C. Donghua, Mechanism of thermal decomposition of cobalt acetate tetrahydrate, *Chem. Pap.* 61 (2007) 329–332. doi:10.2478/s11696-007-0042-3.
- [50] C. Ehrhardt, M. Gjikaj, W. Brockner, Thermal decomposition of cobalt nitrate compounds: Preparation of anhydrous cobalt(II)nitrate and its characterisation by Infrared and Raman spectra, *Thermochim. Acta*. 432 (2005) 36–40. doi:10.1016/j.tca.2005.04.010.
- [51] I. Aarna, E.M. Suuberg, A review of the kinetics of the nitric oxide-carbon reaction, *Fuel*. 76 (1997) 475–491. doi:10.1016/S0016-2361(96)00212-8.
- [52] B.R. Stanmore, V. Tschamber, J.F. Brillhac, Oxidation of carbon by NO_x, with particular reference to NO₂ and N₂O, *Fuel*. 87 (2008) 131–146. doi:10.1016/j.fuel.2007.04.012.
- [53] C. Chen, J. Zhang, F. Peng, D. Su, Efficient functionalization of multi-walled carbon nanotubes by nitrogen dioxide, *Mater. Res. Bull.* 48 (2013) 3218–3222.

doi:10.1016/j.materresbull.2013.04.095.

- [54] I.I. Salame, T.J. Badosz, Surface chemistry of activated carbons: Combining the results of temperature-programmed desorption, Boehm, and potentiometric titrations, *J. Colloid Interface Sci.* 240 (2001) 252–258. doi:10.1006/jcis.2001.7596.
- [55] B.F. Machado, M. Oubenali, M. Rosa Axet, T. Trang Nguyen, M. Tunckol, M. Girleanu, O. Ersen, I.C. Gerber, P. Serp, Understanding the surface chemistry of carbon nanotubes: Toward a rational design of Ru nanocatalysts, *J. Catal.* 309 (2014) 185–198. doi:10.1016/j.jcat.2013.09.016.
- [56] C. Rivera-Cárcamo, I.C. Gerber, I. del Rosal, B. Guicheret, R. Castro Contreras, L. Vanoye, A. Favre-Réguillon, B.F. Machado, J. Audevard, C. de Bellefon, R. Philippe, P. Serp, Control of the single atom/nanoparticle ratio in Pd/C catalysts to optimize the cooperative hydrogenation of alkenes, *Catal. Sci. Technol.* 11 (2021) 984–999. doi.org/10.1039/D0CY01938K.
- [57] W. Xia, C. Jin, S. Kundu, M. Muhler, A highly efficient gas-phase route for the oxygen functionalization of carbon nanotubes based on nitric acid vapor, *Carbon N. Y.* 47 (2009) 919–922. doi:10.1016/j.carbon.2008.12.026.
- [58] Z. Xu, C. Duong-Viet, H. Ba, B. Li, T. Truong-Huu, L. Nguyen-Dinh, C. Pham-Huu, Gaseous nitric acid activated graphite felts as hierarchical metal-free catalyst for selective oxidation of H₂S, *Catalysts*. 8 (2018) 145. doi:10.3390/catal8040145.
- [59] W. Shen, Z. Li, Y. Liu, Surface chemical functional groups modification of porous carbon, recent patents, *Chem. Eng.* 1 (2012) 27–40. doi:10.2174/2211334710801010027.
- [60] M.F.R. Pereira, S.F. Soares, J.J.M. Órfão, J.L. Figueiredo, Adsorption of dyes on activated carbons: Influence of surface chemical groups, *Carbon N. Y.* 41 (2003) 811–821. doi:10.1016/S0008-6223(02)00406-2.
- [61] M.S. Shafeeyan, W.M.A.W. Daud, A. Houshmand, A. Shamiri, A review on surface modification of activated carbon for carbon dioxide adsorption, *J. Anal. Appl. Pyrolysis*. 89 (2010) 143–151. doi:10.1016/j.jaap.2010.07.006.
- [62] U. Zielke, K.J. Hüttinger, W.P. Hoffman, Surface-oxidized carbon fibers: I. Surface structure and chemistry, *Carbon N. Y.* 34 (1996) 983–998. doi:10.1016/0008-6223(96)00032-2.
- [63] S. Kundu, Y. Wang, W. Xia, M. Muhler, Thermal stability and reducibility of oxygen-containing functional groups on multiwalled carbon nanotube surfaces: a quantitative high-resolution XPS and TPD/TPR study, *J. Phys. Chem. C*. 112 (2008) 16869–16878. doi:10.1021/jp804413a.
- [64] A. Barroso-Bogeat, M. Alexandre-Franco, C. Fernández-González, V. Gómez-Serrano, Activated carbon surface chemistry: Changes upon impregnation with Al(III), Fe(III) and Zn(II)-metal oxide catalyst precursors from NO₃⁻ aqueous solutions, *Arab. J. Chem.* 12 (2019) 3963–3976. doi:10.1016/j.arabjc.2016.02.018.
- [65] O. Ducreux, B. Rebours, J. Lynch, M. Roy-Auberger, D. Bazin, Microstructure of supported cobalt Fischer-Tropsch catalysts, *Oil Gas Sci. Technol. - Rev. l'IFP*. 64 (2009) 49–62. doi:10.2516/ogst:2008039.
- [66] G. Kwak, D.-E. Kim, Y.T. Kim, H.-G. Park, S.C. Kang, K.-S. Ha, K.-W. Jun, Y.-J. Lee,

- Enhanced catalytic activity of cobalt catalysts for Fischer–Tropsch synthesis via carburization and hydrogenation and its application to regeneration, *Catal. Sci. Technol.* 6 (2016) 4594–4600.
- [67] E. Patanou, N.E. Tsakoumis, R. Myrstad, E.A. Blekkan, The impact of sequential H₂-CO-H₂ activation treatment on the structure and performance of cobalt based catalysts for the Fischer-Tropsch synthesis, *Appl. Catal. A Gen.* 549 (2018) 280–288. doi:10.1016/j.apcata.2017.10.007.
- [68] V.A. De La Peña O’Shea, P.R. De la Piscina, N. Homs, G. Aromí, J.L.G.G. Fierro, Development of hexagonal closed-packed cobalt nanoparticles stable at high temperature, *Chem. Mater.* 21 (2009) 5637–5643. doi:10.1021/cm900845h.
- [69] C.-H. Chen, C.-C. Huang, Enhancement of hydrogen spillover onto carbon nanotubes with defect feature, *Microporous Mesoporous Mater.* 109 (2008) 549–559. doi:10.1016/j.micromeso.2007.06.003.
- [70] S. ullah Rather, Hydrogen uptake of cobalt and copper oxide-multiwalled carbon nanotube composites, *Int. J. Hydrogen Energy.* 42 (2017) 11553–11559. doi:10.1016/j.ijhydene.2017.03.066.
- [71] M. Aghababaei, A.A. Ghoreyshi, K. Esfandiari, Optimizing the conditions of multi-walled carbon nanotubes surface activation and loading metal nanoparticles for enhanced hydrogen storage, *Int. J. Hydrogen Energy.* 45 (2020) 23112–23121. doi:10.1016/j.ijhydene.2020.06.201.
- [72] A.J. Lachawiec, R.T. Yang, Reverse spillover of hydrogen on carbon-based nanomaterials: evidence of recombination using isotopic exchange, *J. Phys. Chem. C.* 113 (2009) 13933–13939. doi:10.1021/jp903555y.
- [73] R. Bhowmick, S. Rajasekaran, D. Friebel, C. Beasley, L. Jiao, H. Ogasawara, H. Dai, B. Clemens, A. Nilsson, L. Jiao, H. Dai, S. Rajasekaran, D. Friebel, H. Ogasawara, A. Nilsson, C. Beasley, L. Jiao, H. Ogasawara, H. Dai, B. Clemens, A. Nilsson, L. Jiao, H. Dai, S. Rajasekaran, D. Friebel, H. Ogasawara, A. Nilsson, Hydrogen spillover in Pt-single-walled carbon nanotube composites: Formation of stable C-H bonds, *J. Am. Chem. Soc.* 133 (2011) 5580–5586. doi:10.1021/ja200403m.
- [74] Z. Wang, F.H. Yang, R.T. Yang, Enhanced hydrogen spillover on carbon surfaces modified by oxygen plasma, *J. Phys. Chem. C.* 114 (2010) 1601–1609.
- [75] X. Fan, C. Yu, J. Yang, Z. Ling, J. Qiu, Hydrothermal synthesis and activation of graphene-incorporated nitrogen-rich carbon composite for high-performance supercapacitors, *Carbon N. Y.* 70 (2014) 130–141. doi:10.1016/j.carbon.2013.12.081.
- [76] N. Díez, A. Tiwak, S. Gryglewicz, B. Grzyb, G. Gryglewicz, Enhanced reduction of graphene oxide by high-pressure hydrothermal treatment, *RSC Adv.* 5 (2015) 81831–81837. doi:10.1039/c5ra14461b.
- [77] T.W. van Deelen, H. Yoshida, R. Oord, J. Zečević, B.M. Weckhuysen, K.P. de Jong, Cobalt nanocrystals on carbon nanotubes in the Fischer-Tropsch synthesis: Impact of support oxidation, *Appl. Catal. A Gen.* 593 (2020) 117441. doi:10.1016/j.apcata.2020.117441.
- [78] G. Chabot, R. Guilet, P. Cognet, C. Gourdon, A mathematical modeling of catalytic milli-fixed bed reactor for Fischer-Tropsch synthesis: Influence of tube diameter on

- Fischer Tropsch selectivity and thermal behavior, *Chem. Eng. Sci.* 127 (2015) 72–83. doi:10.1016/j.ces.2015.01.015.
- [79] G.L. Bezemer, J.H. Bitter, H.P.C.E. Kuipers, H. Oosterbeek, J.E. Holewijn, X. Xu, F. Kapteijn, A.J. Van Dillen, K.P. De Jong, Cobalt particle size effects in the Fischer-Tropsch reaction studied with carbon nanofiber supported catalysts, *J. Am. Chem. Soc.* 128 (2006) 3956–3964. doi:10.1021/ja058282w.
- [80] A.N. Pour, M. Housaindokht, Effects of metallic cobalt crystal phase on catalytic activity of cobalt catalysts supported on carbon nanotubes in Fischer–Tropsch synthesis, *Prog. React. Kinet. Mech.* 44 (2019) 316–323. doi:10.1177/1468678319862438.
- [81] Y. Yang, L. Jia, B. Hou, D. Li, J. Wang, Y. Sun, The correlation of interfacial interaction and catalytic performance of N-doped mesoporous carbon supported cobalt nanoparticles for Fischer–Tropsch synthesis, *J. Phys. Chem.* 118 (2014) 268–277. doi:10.1021/jp408174w.
- [82] H. Xiong, M.A.M.M. Motchelaho, M. Moyo, L.L. Jewell, N.J. Coville, Cobalt catalysts supported on a micro-coil carbon in Fischer-Tropsch synthesis: A comparison with CNTs and CNFs, *Catal. Today.* 214 (2013) 50–60. doi:10.1016/j.cattod.2012.10.018.
- [83] W. Xie, Y. Zhang, K. Liew, J. Li, Effect of catalyst confinement and pore size on Fischer-Tropsch synthesis over cobalt supported on carbon nanotubes, *Sci. China Chem.* 55 (2012) 1811–1818. doi:10.1007/s11426-012-4727-2.
- [84] J.P. Den Breejen, P.B. Radstake, G.L. Bezemer, J.H. Bitter, V. Frøseth, A. Holmen, K.P. De Jong, V. Frøseth, A. Holmen, K.P. De Jong, V. Frøseth, A. Holmen, K.P. De Jong, On the origin of the cobalt particle size effects in Fischer-Tropsch catalysis, *J. Am. Chem. Soc.* 131 (2009) 7197–7203. doi:10.1016/j.cattod.2008.10.036.J.
- [85] J.X. Liu, H.Y. Su, D.P. Sun, B.Y. Zhang, W.X. Li, Crystallographic dependence of CO activation on cobalt catalysts: HCP versus FCC, *J. Am. Chem. Soc.* 135 (2013) 16284–16287. doi:10.1021/ja408521w.
- [86] I.T. Ghampson, C. Newman, L. Kong, E. Pier, K.D. Hurley, R.A. Pollock, B.R. Walsh, B. Goundie, J. Wright, M.C. Wheeler, R.W. Meulenberg, W.J. Desisto, B.G. Frederick, R.N. Austin, Effects of pore diameter on particle size, phase, and turnover frequency in mesoporous silica supported cobalt Fischer-Tropsch catalysts, *Appl. Catal. A Gen.* 388 (2010) 57–67. doi:10.1016/j.apcata.2010.08.028.
- [87] J. Xiao, X. Pan, S. Guo, P. Ren, X. Bao, Toward fundamentals of confined catalysis in carbon nanotubes, *J. Am. Chem. Soc.* 137 (2015) 477–482. doi:10.1021/ja511498s.
- [88] A.M. Saib, D.J. Moodley, I.M. Ciobîc, M.M. Hauman, B.H. Sigwebela, Fundamental understanding of deactivation and regeneration of cobalt Fischer-Tropsch synthesis catalysts, *Catal. Today.* 154 (2010) 271–282. doi:10.1016/j.cattod.2010.02.008.
- [89] E. Rytter, A. Holmen, Deactivation and regeneration of commercial type Fischer-Tropsch Co-catalysts - A mini-review, *Catalysts.* 5 (2015) 478–499. doi:10.3390/catal5020478.
- [90] M. Khorashadizadeh, H. Atashi, Modeling the kinetics of cobalt Fischer-Tropsch catalyst deactivation trends through an innovative modified Weibull distribution, *Phys. Chem. Chem. Phys.* 19 (2017) 19252–19261. doi:10.1039/c7cp02210g.

- [91] A. Nakhaei, P. Elham, H. Mostafa, Prediction of cobalt particle size during catalyst deactivation in Fischer-Tropsch synthesis, *J. Iran. Chem. Soc.* 13 (2015) 139–147. doi:10.1007/s13738-015-0721-x.
- [92] M. Trépanier, A. Tavasoli, S. Anahid, A. K. Dalai, Deactivation behavior of carbon nanotubes supported cobalt catalysts in Fischer-Tropsch synthesis, *Iran. J. Chem. Chem. Eng.* 30 (2011) 37–47.
- [93] J. Park, Y. Lee, P.R. Karandikar, K. Jun, K. Ha, H. Park, Fischer – Tropsch catalysts deposited with size-controlled Co_3O_4 nanocrystals : Effect of Co particle size on catalytic activity and stability, *Appl. Catal. A, Gen.* 411–412 (2012) 15–23. doi:10.1016/j.apcata.2011.10.010.
- [94] M. Wolf, H. Kotzé, N. Fischer, M. Claeys, Size dependent stability of cobalt nanoparticles on silica under high conversion Fischer–Tropsch environment, *Faraday Discuss.* 197 (2017) 243–268. doi:10.1039/C6FD00200E.
- [95] N.E. Tsakoumis, M. Rønning, Ø. Borg, E. Rytter, A. Holmen, Deactivation of cobalt based Fischer-Tropsch catalysts: a review, *Catal. Today.* 154 (2010) 162–182. doi:10.1016/j.cattod.2010.02.077.
- [96] J.M. González-Carballo, S. Sadasivan, P. Landon, R.P. Tooze, Synthesis of cobalt nanodumbbells and their thermal stability under H_2 , H_2/CO and O_2 atmospheres, *Mater. Charact.* 118 (2016) 519–526. doi:10.1016/j.matchar.2016.06.031.
- [97] S. Lyu, B. Peng, T. Kuang, K.G. Rappé, Y. Zhang, J. Li, L. Wang, Supported cobalt nanoparticles with a single active phase for Fischer-Tropsch synthesis, *ACS Appl. Nano Mater.* 2 (2019) 2266–2272. doi:10.1021/acsanm.9b00187.
- [98] M.K. Gnanamani, G. Jacobs, W.D. Shafer, B.H. Davis, Fischer-Tropsch synthesis: Activity of metallic phases of cobalt supported on silica, *Catal. Today.* 215 (2013) 13–17. doi:10.1016/j.cattod.2013.03.004.
- [99] J. Harmel, L. Peres, M. Estrader, A. Berliet, S. Maury, A. Fécant, B. Chaudret, P. Serp, K. Soulantica, hcp-Co nanowires grown on metallic foams as catalysts for the Fischer-Tropsch synthesis, *Angew. Chem.* 57 (2018) 10579–10583. doi:10.1002/anie.201804932.

Table of Contents/Abstract Graphics

